ON THE MAPPING OF MULTIVARIATE GEOPHYSICAL FIELDS: SENSITIVITIES TO SIZE, SCALES AND DYNAMICS

P.F.J. Lermusiaux
Harvard University

Abstract

The effects of *a priori* parameters on the error subspace estimation and mapping methodology introduced in Lermusiaux *et al.* (2000) is investigated. The approach is three-dimensional, multivariate and multiscale. The sensitivities of the subspace and *a posteriori* fields to the size of the subspace, scales considered and nonlinearities in the dynamical adjustments are studied. Applications focus on the mesoscale to subbasin-scale physics in the northwestern Levantine during February 10-March 15 and March 19-April 16, 1995. Forecasts generated from various analyzed fields are compared to *in situ* and satellite data. The sensitivities to size show that the truncation to a subspace is efficient. The use of criteria to determine adequate sizes is emphasized and a back-of-the-envelope rule is outlined. The sensitivities to scales confirm that, for a given region, smaller scales usually require larger subspaces because of spectral redness. However, synoptic conditions are also shown to strongly influence the ordering of scales. The sensitivities to the dynamical adjustment reveal that nonlinearities can modify the variability decomposition, especially the dominant eigenvectors, and that changes are largest for the features and regions with high shears. Based on the estimated variability variance fields, eigenvalue spectra, multivariate eigenvectors and (cross)-covariance functions, dominant dynamical balances and the spatial distribution of hydrographic and velocity characteristic scales are obtained for primary regional features. In particular, the Ierapetra is found to be close to gradient-wind balance and coastal-trapped waves are anticipated to occur along the northern escarpment of the basin.

Journal of Atmospheric and Oceanic Technology

In Press

January 14, 2002

1. INTRODUCTION

In mapping geophysical fields and their uncertainties, it is important to assess the sensitivity to parameters. The present work carries out such studies for the *a priori* error subspace estimation and mapping methodology introduced in (Lermusiaux *et al.*, 2000, henceforth, LAL00). With this three-dimensional, multivariate and multiscale approach (App. A), the *a priori* error subspace, i.e. the dominant components of the *a priori* missing variability or probability density functions of the state to be mapped, are constructed in two parts. The observed portions of the subspace are specified based on measurements and multiscale statistical models. The non-observed portions are then built by dynamical adjustments to the observed portions. Once this *a priori* error subspace is computed, the data sets of interest can be mapped into gridded fields and error properties by Bayesian estimation in the subspace. Presently, error statistics are assumed to be described by covariance matrices and the mapping (analysis) reduces to a minimum error variance estimation problem. The subspace is then determined by the dominant eigendecomposition of the *a priori* error covariance.

Two main objectives are to investigate (i) the sensitivity of the state and error estimates to the properties of the subspace (e.g. size, dynamics, adjustment) and (ii) the sensitivity of the subspace itself to its size and to the data and dynamics utilized in its construction. The types of questions considered include: How many, and why so many, eigenvectors should be employed to represent most of a covariance matrix or to carry out a mapping? How sensitive is the subspace to the parameters of the model employed in its dynamical adjustment? By how much should such subspaces be dynamically adjusted? And finally, what is the performance of forecasts generated from these analyses? Results obtained from different *a priori* parameters are compared among each other and also to those of the univariate horizontal (2D) scheme of the Harvard Ocean Prediction System (HOPS, Lozano *et al.*, 1996; Robinson, 1996). Since this benchmark is multiscale, the present 3D mapping of fields and error covariances is referred to in short as the "multivariate 3D" scheme. Ultimately, forecasts generated from the various analyses are compared to *in situ* and satellite data, using root-mean-square differences and correlation coefficients for measures of skill. The third objective is to extract dynamical knowledge from the variability subspaces and fields computed. This is carried out by studying the spatial distribution of the estimated hydrographic and velocity variances, shapes and amplitudes of dominant multivariate eigenvectors, and structures of (cross)-covariance functions.

The applications illustrated are in the Levantine sea and focus on the mesoscale to subbasin-scale physical errors and fields. The measurements were collected during the LIW95 campaign (Roether *et al.*, 1996; Malanotte-Rizzoli *et al.*, 1996) carried out from January to April 1995 in the Eastern Mediterranean. To introduce this region and its contemporary upper-thermocline features, a multivariate 3D estimate of the potential density at 105 m and velocity at 5 m is plotted on Fig. 1. Because of thermal-wind effects, several surface circulation structures are easily distinguished along the steepest slopes of isopycnals. To date, most investigations in the Levantine that combine data and dynamics have mainly resolved the subbasin-scales and are usually based on close-to-geostrophy hypotheses (e.g. Hecht *et al.*, 1988; Milliff and Robinson, 1992; Özsoy *et al.*, 1993; Robinson and Malanotte-Rizzoli, 1993; Malanotte-Rizzoli *et al.*, 1999).

Among the various techniques for the analysis of geophysical fields, only some estimate uncertainties (LAL00 and references cited therein). The present work is concerned with determining accurate *a priori* (error) covariance or structure functions, and estimating their parameters and covariance matrix form. Recent studies include: in atmospheric science, Rabier *et al.* (1998), Riishojgaard (1998), Dee and da Silva (1999), Gaspari and Cohn (1999), Gneiting (1999), Franke and Barker (2000); in physical oceanography, Cressie and Huang (1999), Miller and Cornuelle (1999), Menemenlis and Chechelnitsky (2000), Molinari and Festa (2000); and, in biological oceanography, Abbott and Letelier (1998). Today, error models, in particular the efficient representation of error covariance matrices, are essential for error predictions (Ehrendorfer, 1997; Lermusiaux, 1997, henceforth, LER97) and data assimilation (Robinson *et al.*, 1998; Chin *et al.*, 1999; Derber and Bouttier, 1999; Lermusiaux, 1999a,b; Lermusiaux and Robinson, 1999; Verron *et al.*, 1999; Keppenne, 2000; Mitchell and Houtekamer, 2000; Tippett *et al*, 2000; Hamill *et al.*, 2001; Reichle *et al.*, 2002).

In what follows, Sect. 2 outlines a simple rule for estimating the size of error subspaces. In Sect. 3, variations of these subspaces with their size and with the scales in the data, and the impacts of these variations on *a posteriori* fields, are illustrated for temperature and salinity. Sect. 4 proceeds to the complete physics: in addition to size and scales, nonlinear effects are studied and some dynamical properties derived. In Sect. 5, the performance of forecasts initialized based on the present mapping is evaluated. Conclusions are in Sect. 6. In the Appendices, algorithms are summarized and relevant non-dimensional numbers listed.

2. THE SIZE OF ERROR SUBSPACES: BACK-OF-THE-ENVELOPE CALCULATION

A simple rule giving an approximate order of magnitude for the size of multivariate error subspaces is outlined. It is based on experience with more quantitative calculations (e.g. Fukumori and Malanotte-Rizzoli, 1995; LER97, Lermusiaux, 1999a,b) and on the often red spectra of ocean phenomena. It is exemplified for the case where errors are mesoscale variability.

Consider first one state variable, e.g. temperature or zonal velocity. For the vertical variability, 2 to 3 empirical orthogonal functions (EOFs) or dynamical modes often explain most of the significant variance (e.g. De Mey and Robinson, 1987; Haney *et al*, 1995; De Mey, 1997; Wunsch, 1997; Pedder and Gomis, 1998; von Storch and Frankignoul, 1998). For the horizontal variability, most studies to date focus on surface fields. In that case, the number of dominant patterns or modes usually varies between 15 to about 50: for example, consider a surface field in the Gulf Stream or Atlantic region (e.g. Thacker and Lewandowicz, 1996, 1997; Everson *et al.*, 1997; Kaplan *et al.*, 1997). For the 3D variability, an approximate subspace size is simply the product of vertical and horizontal requirements. With the above values, this product yields a size of 30 to 150.

In the case of several state variables, the size of the subspace necessary to describe most of a normalized form of the multivariate variability is often found proportional to the number of variables. With this hypothesis, considering for example the primitive equation (PE) model[1] of HOPS and the above mesoscale values, an approximate size is then 135 to 650. This is of the order of 10^2 to 10^3. In summary, the order of magnitude of the size p of an error subspace is often well approximated by,

$$\mathcal{O}(p) \simeq \sum_v n_h^v \times n_z^v \ , \tag{1}$$

where n_h^v (n_z^v) is an estimate of the horizontal (vertical) requirements for the state variable v. Similarly, a range of likely p is obtained from the products of the minimum and maximum horizontal and vertical requirements, i.e. $\sum_v \min(n_h^v \times n_z^v) \leq p \leq \sum_v \max(n_h^v \times n_z^v)$. Such back-of-the-envelope rules don't require extensive 3D computations. They are very useful today since they provide quick estimates of the number of state samples, breed vectors or

[1] This dynamical PE model governs five state variables, henceforth called the "PE fields": four three-dimensional fields, the temperature T, salinity S and internal horizontal velocities $\widehat{u}$ and $\widehat{v}$ (zonal x and meridional y directions), and one two-dimensional field, the barotropic transport stream function ψ. The main model parameters are in Lermusiaux *et al.* (1998), henceforth, LLA98.

singular vectors (e.g. Molteni *et al.* 1996; Toth and Kalnay, 1997; Barkmeijer *et al.* 1998) needed to explain most of the variance in an analysis or ensemble forecast.

The above sizes are much larger than classic 1D requirements but much smaller than the number of discrete state variables. For example, consider a non-dimensional (from here on denoted by *) covariance matrix $\mathbf{B}^*$ for a horizontal, univariate field. For covariance function, we use a "Mexican hat"[2] and for discretized domain, the northwestern Levantine with a uniform resolution of 10 km (500 km in the x and 520 km in the y direction). The size of $\mathbf{B}^*$ is thus $[2703 \times 2703]$. Computing its cumulative eigenvalue spectrum for the subbasin-scales (200 km zero-crossing, 100 km decay-scale), 15 eigenvectors represent 85% of the variance, 36 vectors 99% and 50 vectors 99.8%. For the mesoscales (60 km zero-crossing, 30 km decay-scale), larger numbers are required: 15 eigenvectors represent 20% of the variance, 50 vectors 56% and 100 vectors 83%. For at least 90% of the variance, 19 vectors are necessary for the subbasin-scales and 128 for the mesoscales. These sizes only represent 0.7% and 4.7% of the number of discrete state variables, 2703, respectively. Illustrations and further details are in LLA98.

3. MULTIVARIATE THREE-DIMENSIONAL ANALYSIS OF TRACER FIELDS: SUBSPACE SIZE

Hydrographic data (dynamical tracers T and S) are frequent observations. The sensitivity of the *a posteriori* state $\mathbf{x}^{\mathrm{a}}_{\mathrm{trc}}$ to the size of the *a priori* error subspace is thus first exemplified for the case of a global mapping of temperature and salinity. The subspace is constructed assuming that the *a priori* error covariance of these tracers $\mathbf{B}_{\mathrm{trc}}$ is "observed" in the sense of LAL00, i.e. historical (synoptic) data are available to specify its dominant eigendecomposition $\mathbf{B}^p_{\mathrm{trc}}$. Variations of $\mathbf{B}^p_{\mathrm{trc}}$ with the scales considered are illustrated. Some differences between our multivariate 3D scheme and Kalman update (App. A.3) are also exemplified.

The data are 146 T and S profiles (Fig. 2a-b). Their error model (App. A) includes a decorrelation time term. The numerical domain (Fig. 2c) contains 2703 horizontal grid points and 20 vertical levels (108120 tracer state variables). There are 5840 data-points (dimension of $\mathbf{y}^{\mathrm{o}}$, eq. A1b), i.e. the number of T, S scalar data residuals on vertical levels.

---

[2] This is the negative of the second derivative of a 2D Gaussian function (e.g. Carter and Robinson, 1987; Louis *et al.*, 1997). Parameters are the zero-crossing l_a, e-folding decay-scale l_b and decorrelation time τ. Elements of $\mathbf{B}^*$ are of the form $C^*(\mathbf{r}_1, \mathbf{r}_2) = (1 - a^2)\ e^{-b^2/2}$, where $a^2 = (\mathbf{r}_1 - \mathbf{r}_2)^T \mathbf{L}_a^{-2} (\mathbf{r}_1 - \mathbf{r}_2)$ and $b^2 = (\mathbf{r}_1 - \mathbf{r}_2)^T \mathbf{L}_b^{-2} (\mathbf{r}_1 - \mathbf{r}_2) + (\Delta t_i/\tau)^2$ are scalars, and $\mathbf{r}_1$ and $\mathbf{r}_2$ horizontal position vectors, with $\mathbf{r} = (x, y)$. The 2-by-2 matrix $\mathbf{L}_a$ contains l_a on its diagonal; $\mathbf{L}_b$ contains l_b. The decorrelation time term, in which Δt_i is the interval between the data time t_i and estimation time t_0, is part of the measurement error model (App. A).

The benchmark univariate 2D scheme of HOPS assumes that two independent scales are present and that errors are homogeneous horizontally. It uses a successive correction, minimum error variance technique (e.g. Daley, 1991; Lorenc, 1992): the largest scales are gridded first and the resulting fields constitute the background in the mapping of smaller scales. Successively for each scale, global horizontal analyses of scale-filtered T and S data are thus carried out at various levels. For fair comparisons with this benchmark, the present multivariate 3D scheme is also a two-scale correction ($w = 1, 2$ in Apps. A.2–3), with horizontally homogeneous *a priori* errors. It thus carries out two multivariate 3D mappings successively. For each scale, $\mathbf{B}^{p}_{\rm trc}$ is constructed based on a statistical model fit to data in the horizontal and on data EOFs in the vertical (App. A, Table A.a). In this Section, the data used to do so is $\mathbf{y}^{\rm o}$. For both schemes, the first *a priori* estimate $\mathbf{x}^{\rm b}_{\rm trc}$ ($w = 0$ in Apps. A.2–3) is the horizontal average of $\mathbf{y}^{\rm o}$. Subsequently, the two scales are the subbasin-scale and mesoscale. At the mesoscale stage (Sect. 3.2), *a priori* errors are mesoscale variability but *a posteriori* fields are the total fields.

3.1 Subbasin-scale

Univariate 2D benchmark. Figure 3 shows four subbasin-scale ($w = 1$) univariate 2D analyses. The *a priori* horizontal covariance was set to be a "Mexican hat" (Sect. 2) of 200 km zero-crossing and 100 km decay-scale, each estimated based on covariances among subbasin-scale data residuals. The data error covariance at data-points was assumed diagonal (at each level, $\mathbf{R} = r\mathbf{I}$) and of 50 days decorrelation time-scale. The corresponding horizontally uniform, non-dimensional (0 to 1) variance was calibrated to $r^* = 0.03$, mainly based on experience.

Multivariate 3D scheme. Figure 4 illustrates the construction of $\mathbf{B}_{\rm trc}$ and Fig. 5 the mappings. The dominant eigendecomposition of $\mathbf{C}^{z}_{\rm trc}$ (eq. A10) is computed based on the EOFs of the subbasin-scale data residuals (eqs. A7–A9). A small number of T, S EOFs explains most of the variance (Fig. 4a). The horizontal covariance $\mathbf{C}^{\mathbf{r}^*}_{\rm trc}$ (eq. A11) is analytical, computed based on the subbasin-scale Mexican hat used in the univariate 2D analyses. From (eqs. A13–15), the vertical (eq. A10) and horizontal (eq. A12) decompositions are then combined. The resulting normalized variance is explained by a few hundred 3D vectors (Fig. 4b). Using (eq. A16) in (App. A.3), the subbasin-scale mapping ($w = 1$) is finally carried out.

Figure 5a plots parts of the state $\mathbf{x}^{\rm a}_{\rm trc}$ for the case where $p = 500$ in (eq. A16), i.e 500 eigenvectors are used which explains 99.6% of the *a priori* error variance (Fig. 4b). The size

of $\mathbf{x}^{\mathrm{a}}_{\mathrm{trc}}$ being 108120, this analysis is 216 times cheaper than a full covariance formulation and about 12 times cheaper than a Representer method (Bennett and Chua, 1994), the number of Representers being 5840. Comparing results (Figs. 5a and 3), the T, S maps are alike. For the subbasin-scale, assuming zero vertical covariance and uncorrelated T and S error fields does not appear damaging. This is mainly because there is here more than enough data coverage for the subbasin-scale. The vertical and T–S correlations are as expected stronger with the 3D scheme (Fig. 5a), but differences are within data error bounds.

Comparing the T, S maps using 500 and 250 vectors (not shown), the relative Root Mean Square (RMS) differences are less than 1%. This is an interesting result. Once most (e.g. here $\geq 98\%$, see Fig. 4b) of the covariance has converged, the remaining eigenvectors can be ignored if their eigenvalues are negligible in comparison to data error eigenvalues (LLA98). Considering costs, the mapping with $p = 250$ would be 10^3 times cheaper than the full covariance mapping. Finally, using 10 vectors as on Fig. 5b is not sufficient. Indeed, the quick product of horizontal and vertical requirements for 99% of the variance each indicates here a total of $36 \times 8 = 288$ vectors (see eq. 1 and use numbers in Sect. 2 and Fig. 4a). This back-of-the-envelope order of 10^2 multivariate 3D vectors agrees with the numerically computed spectra of Fig. 4b.

3.2 Mesoscale

Univariate 2D benchmark. Figure 6 shows four mesoscale ($w = 2$) univariate 2D analyses. Based on plots of covariances among data residuals, the zero-crossing was set at 60 km, decay-scale at 30 km and decorrelation time-scale at 7 days. Other parameters are as in Sect. 3.1.

Multivariate 3D scheme. In the mesoscale 3D mapping, $\mathbf{x}^{\mathrm{b}}_{\mathrm{trc}}$ is the subbasin-scale state of Fig. 5a. The construction of the mesoscale $\mathbf{B}_{\mathrm{trc}}$ is illustrated by Fig. 7. In the vertical (Fig. 7a), the variance of the mesoscale data residuals (eq. A10) decays less rapidly with the eigenvalue number than in the subbasin-scale case (Fig. 4a). In the horizontal, $\mathbf{C}^{\mathbf{r}^*}_{\mathrm{trc}}$ (eq. A11) is computed based on the mesoscale Mexican hat of the univariate 2D analyses. From (eqs. A13–15), the vertical (eq. A10) and horizontal (eq. A12) decompositions are then combined. The resulting normalized mesoscale variance (Fig. 7b) is mostly explained by a few 3D vectors, but compared to the subbasin-scale (Fig. 4b), slightly more vectors are needed. Using (eq. A16) in (App. A.3), the mesoscale mapping ($w = 2$) is finally carried out.

Figures 8a–b show $\mathbf{x}^{\mathrm{a}}_{\mathrm{trc}}$ obtained using the dominant 500 and 750 mesoscale vectors, respectively. Differences with the fields of Fig. 6 are small, at several locations within data error bounds. However, the 3D scheme which uses the significant EOFs of the mesoscale residuals (eqs. A7–10) yields larger vertical correlations. For example, in the upper 0 to 50 m mixed-layer, the measurement noise and unresolved vertical scales are filtered more on Figs. 8a–b. Small mid-depth features of significant vertical extension, e.g. see T, S around 225 m, also seem better represented. For mesoscale mappings with data resolutions similar to those of Fig. 2a, a disadvantage of the univariate 2D analysis is in fact its sensitivity to environmental noise. Considering subspace sizes, the relative RMS differences between maps of Figs. 8a and 8b are less than 3%. Even though 750 vectors explain 5% more *a priori* mesoscale variance than 500 vectors do (Fig. 7b), most of the additional 250 vectors have eigenvalues smaller than the local data error variance. They thus mainly yield mesoscale corrections within data error bounds.

For the 3D scheme, two main properties have been exemplified. First, once most of the *a priori* error covariance has converged (e.g. 99%), the remaining eigenvectors can be truncated in most cases. Second, the *a priori* error vectors of eigenvalues negligible with respect to data errors have negligible impacts on the *a posteriori* state. Even if the *a priori* error covariance has not converged, these vectors can usually be omitted.

4. MULTIVARIATE THREE-DIMENSIONAL ANALYSES OF PE FIELDS

Primitive equation fields and errors are now considered. Examples remain in the northwestern Levantine, but the period is now March 19 to April 16, 1995. Four cases are discussed (Table 1): one univariate 2D benchmark and three variations of the multivariate 3D scheme.

Table 1. The four analyses selected and their main differences

Case	Scheme Employed	Size of *a priori* Error Subspace	Velocity Covariances	Velocity Dynamics Utilized
1:	Univariate 2D (benchmark)	full covariances (all 2D vectors)	Not built: direct integration of thermal-wind equations	Geostrophy
2:	Multivariate 3D	$p = 322$	Built via an ensemble of adjustment PE integrations	Linear momentum PE model
3:	Multivariate 3D	$p = 322$	As above	Nonlinear momentum PE model
4:	Multivariate 3D	$p = 400$	As above	Nonlinear momentum PE model

The univariate 2D benchmark (Case 1) first carries out horizontal analyses for T and S, as in Sect. 3. Total velocity is then computed by assuming geostrophic balance with the gridded tracers and integrating the thermal-wind equations up and down from a level of reference.

The present multivariate 3D scheme (Cases 2–4) also uses a two-scale approach ($w = 1, 2$ in App. A.2) to construct the *a priori* error subspace. For each scale, the tracer portion $\mathbf{B}_{\rm trc}$ of the *a priori* error covariance $\mathbf{B}$ is specified as in Sect. 3. The non-observed velocity portions are then built in dynamical accord with $\mathbf{B}_{\rm trc}$, through an ensemble of adjustment momentum integrations (tracers are kept fixed in these adjustments, see App. A., Table A.b). These integrations lead to an ensemble of PE adjusted fields. Variability samples, i.e. the differences between these fields and *a priori* state $\mathbf{x}^{\rm b}$, are then computed, normalized and organized by singular value decomposition (SVD). Once a convergence criterion determines that the number of samples is large enough to explain most of the variance, an estimate $\mathbf{B}^p$ of $\mathbf{B}$ is obtained. A mapping (App. A.3) is then carried out.

The 3D cases of Table 1 were selected to illustrate the main tendencies in an extensive set of computations. They exemplify the sensitivities of the error subspace and state $\mathbf{x}^{\rm a}$ to: (i) the nonlinear terms of the momentum equations used to adjust the non-observed velocity variability to the observed tracer variability (Cases 2 and 3), and (ii) the size of the subspace p (Cases 3 and 4). Subbasin-scale estimates are only overviewed (Sect. 4.1). Mesoscale estimates are studied in more detail: *a priori* error covariances $\mathbf{B}^p = \mathbf{E}\boldsymbol{\Pi}\mathbf{E}^T$ (Sect. 4.2), *a posteriori* fields (Sect. 4.3), and *a posteriori* error covariances $\mathbf{B}^{{\rm a}^p} = \mathbf{E}^{\rm a}\boldsymbol{\Pi}^{\rm a}\mathbf{E}^{{\rm a}^T}$ (Sect. 4.4). The dynamical possibilities raised by the study of subspaces are emphasized in Sects. 4.2 and 4.4.

4.1 Subbasin-scale

In each case (Table 1), the data $\mathbf{y}^{\rm o}$ employed for the subbasin-scale are 512 profiles of the MODB winter climatology for the Levantine (Brankart, personal communication) and the T/S profiles for February 10–18 and March 15 (Fig. 2a). For coherence with the recent evolution of deep Eastern Mediterranean waters (Roether *et al.*, 1996), the MODB data were cut at 1250 m depth: only *in situ* data are utilized below 1250 m. In all cases, $\mathbf{x}^{\rm b}$ is in hydrostatic equilibrium: its tracer fields are the horizontal averages of the data $\mathbf{y}^{\rm o}$ and its velocity is null.

For the univariate 2D scheme (Case 1), T and S are estimated from $\mathbf{y}^{\rm o}$ as in Sect. 3.1. Total velocities are assumed in geostrophic balance, with a level of no motion at 600 m. For the multivariate 3D Cases 2–4, the $\mathbf{B}^p_{\rm trc}$'s are also as in Sect. 3.1, except for the different sizes p. Three estimates of the subbasin-scale $\mathbf{B}^p$ are then built using the PE model, as indicated in Table 1. With these $\mathbf{B}^p$'s, three mappings of the data $\mathbf{y}^{\rm o}$ are carried out, following (App. A.3).

4.2 Mesoscale: data and *a priori* error covariance

For each case (Table 1), the data for the mesoscale correction are 236 CTD profiles gathered from March 19 to April 16 (Fig. 9). They lead to 9440 data-points (dimension of $\mathbf{y}^{\mathrm{o}}$). To have an acceptable synoptic coverage (see Sect. 5), the field estimation is centered on March 27. The data decorrelation time-scale is adjusted to 7 days.

The four $\mathbf{x}^{\mathrm{b}}$'s (Cases 1 to 4) are the four subbasin-scale fields of Sect. 4.1. Their *a priori* error is thus mesoscale variability: i.e. for Cases 2 to 4, $\boldsymbol{\Gamma} = \mathbf{I}$ in (eq. A23). The corresponding covariances are computed using all 289 CTD profiles gathered from Feb. 10 to April 16 (denoted by $\mathbf{y}^{\mathrm{o}}_{\mathrm{ctd}}$). These four covariance estimations are now described.

Univariate 2D benchmark. Based on plots of covariances among mesoscale residuals of the 289 CTD, the zero-crossing, decay-scale and data decorrelation time-scale are adjusted on basin average to 60 km, 30 km and 7 days. Other parameters of the error covariance function for T and S (see Fig. 9b) are as in Sect. 3.1. Velocity error covariances are not computed.

Multivariate 3D scheme. In constructing the mesoscale $\mathbf{B}^p = \mathbf{E}\boldsymbol{\Pi}\mathbf{E}^T$, the dominant decomposition of its tracer submatrix, $\mathbf{B}^p_{\mathrm{trc}} = \mathbf{E}_{\mathrm{trc}}\boldsymbol{\Pi}_{\mathrm{trc}}\mathbf{E}^T_{\mathrm{trc}}$, is computed first (App. A, Table A.a). This is done by combining the vertical EOFs of the mesoscale tracer residuals ($\mathbf{y}^{\mathrm{o}}_{\mathrm{ctd}_i} - \mathcal{H}_i(\mathbf{x}^{\mathrm{b}})$, $i = 1, \ldots, 289$, eq. A7) with the eigendecomposition of an analytical horizontal tracer covariance (of elements specified using the mesoscale Mexican hat of the benchmark). The resulting cumulative error variance is a curve similar to that of Fig. 7b. For the sizes p utilized (Table 1), the dominant 322 tracer eigenvectors explain 67.2% of the total tracer variance, the dominant 400, 72%, and dominant 500, 76.5%. The complete $\mathbf{B}^p$'s are then obtained from $\mathbf{B}^p_{\mathrm{trc}}$, by adjustment momentum integrations (App. A, Table A.b). The $j = 1, \ldots, p$ dynamical adjustments lasted for 2 model-days, with p increasing based on the convergence criterion $\rho \geq \alpha$ (eq. A22), with the limit α set to 0.93. This coefficient $\rho \leq 1$ assesses the added value of new parallel batches of adjustment runs; some of its values are listed in Table 2.a.

Table 2. Convergence of and similarity between error subspaces

a. Convergence coefficient			
for Case 2:	$\rho_{254-288} = 0.919$	$\rho_{288-322} = 0.930$	
for Case 3:	same values as for Case 4.		
for Case 4:	$\rho_{288-322} = 0.928$	$\rho_{322-360} = 0.929$	$\rho_{360-400} = 0.935$
b. Similarity coefficient			
between Cases 2–3:	$\rho = 0.973$		
between Cases 2–4:	$\rho = 0.845$		
between Cases 3–4:	$\rho = 0.868$		

For Case 2, $\rho \geq \alpha$ was achieved after 322 runs, for $p = 322$ and $\tilde{p} = 288$. For Case 4, 400 runs were necessary, based on $p = 400$ and $\tilde{p} = 360$. This larger dimension is due to the nonlinear momentum terms which create flow variability not estimated by the linear adjustments of Case 2. Since Case 3 is simply the nonlinear extension of Case 2, convergence is not an objective. Overall, the rate of increase of ρ diminishes as $\tilde{p} \leq p$ grows: this is partly because the singular values of $\mathbf{B}$ decay rapidly.

Table 2.b estimates the overall similarity among the three $\mathbf{B}^p$'s, using (eq. A22). Comparing Cases 2 and 3, averaged on volume and state variables, nonlinear momentum terms only change about 2.7% of the non-dimensional PE mesoscale variability. Since here $\mathbf{u}^j = \sqrt{p}\mathbf{e}^j$ in (eq. A17), the tracer covariance in a $\mathbf{B}^p$ is exactly $\mathbf{B}^p_{\rm trc}$. Therefore, the covariances involving total velocities in Cases 2 and 3 differ by about $(1-\rho)n/n_{\rm vel} = 5.4\%$, where n is the state vector size (218,943) and $n_{\rm vel}$ the number of velocity variables (110,823). This 5.4% difference measures the volume-averaged effect of nonlinear momentum terms on velocity covariances. Comparing Cases 3 and 4, they are about 13.2% apart. The tracer eigenvectors of high number (small eigenvalues) here affect velocity covariances[3]. Finally, comparing Cases 2 and 4, their differences combine the nonlinear and size effects (2.7% and 13.2%).

The three $\mathbf{B}^p = \mathbf{E}\boldsymbol{\Pi}\mathbf{E}^T$'s (Cases 2–4) are now compared locally, focusing on variances (Sect. 4.2.a), eigenvectors (Sect. 4.2.b) and covariance functions (Sect. 4.2.d). These estimates substantially improve the univariate 2D scheme which only provides 2D error variance fields.

4.2.a A priori mesoscale error variance

Univariate 2D benchmark. *A priori* tracer error variances are set to the horizontally-averaged variance of the residuals of $\mathbf{y}^{\rm o}_{\rm ctd}$: they are depth-dependent. The corresponding velocity error variances are set assuming geostrophic balance.

Multivariate 3D scheme. Error variances form the diagonal of the $\mathbf{B}^p$'s. Tracer variances are horizontally uniform in the data domain (Fig. 9). For Cases 2 and 3 ($p = 322$), the T/S error standard deviation at 5 m is 0.40°C/0.080 PSU, while at 500 m, it is 0.17°C/0.039 PSU. For Case 4 (see LAL00), standard deviations are logically slightly larger: to first order[4], using

[3] This 13.2% rise is partly due to the 4.8% increase in normalized 3D tracer variance explained (from 67.2% at $p = 322$ to 72% at $p = 400$).

[4] To link ratios of standard deviations to ratios of variances, one can use: $\frac{x_2^2 - x_1^2}{2x_2^2} \leq \frac{x_2 - x_1}{x_2} \leq \frac{x_2^2 - x_1^2}{2x_1^2}$ with $x_2 > x_1 > 0$.

the variance numbers given above, by 3.3% to 3.6% ($100 \times (72 - 67.2)/2$, divided by 72 and 67.2). Total velocity variances are non-uniform in 3D. By construction, large *a priori* errors (Table 3) correspond to the locations and features estimated to have large mesoscale flow variability. They reflect local variations of the dominant density and momentum balances.

Table 3. *A priori* mesoscale error standard deviations (St.Dv.) for velocity: estimates of Cases 2 and 3/4

Case	Depth	Features (and horizontal averages)	ψ error St.Dv.	Internal velocity error St.Dv.
2.	Surface	Above the Rhodes basin:	0.85 Sv	15.5 cm s^{-1}
	(5 m)	Ierapetra:	0.8 Sv	14.5 cm s^{-1}
		Mersa Matruh Gyre:	0.8 Sv	13 cm s^{-1}
		Mid-Mediterranean Jet:	0.68 Sv	13.5 cm s^{-1}
		Surface average:	0.65 Sv	12.5 cm s^{-1}
	500 m	Kasos and Karpathos Straits:		1.7 cm s^{-1}
		Above the Rhodes basin:		1.3 cm s^{-1}
		500 m average:		0.65 cm s^{-1}
3./4.	Surface	Ierapetra:	0.87/0.9 Sv	22/23 cm s^{-1}
	(5 m)	Above the Rhodes basin:	0.87/0.9 Sv	16/16 cm s^{-1}
		Mersa Matruh Gyre:	0.84/0.86 Sv	17/18 cm s^{-1}
		Mid-Mediterranean Jet:	0.69/0.72 Sv	14/15 cm s^{-1}
		Surface average:	0.67/0.7 Sv	13.5/14 cm s^{-1}
	500 m	Kasos and Karpathos Straits:		1.75/1.8 cm s^{-1}
		Above the Rhodes basin:		1.4/1.5 cm s^{-1}
		Ierapetra:		0.95/1 cm s^{-1}
		Anticyclone in MM-S-G complex:		1/1.05 cm s^{-1}
		500 m average:		0.68/0.7 cm s^{-1}

In Case 2 (linear momentum), at the surface, the largest standard deviations are as expected above the Rhodes basin (flanked by steep topography) within the deep, subbasin-scale Rhodes Gyre. Other features of above average flow variability are, in decreasing order, the Ierapetra, Mersa Matruh Gyre (one of its lobes is in the domain) and central branch of the Mid-Mediterranean Jet. At 500 m depth, the largest $\widehat{u}, \widehat{v}$ deviations are near the inflow/outflow of the Kasos and Karpathos Straits, and again above the Rhodes basin.

In Case 3 (nonlinear momentum, $p = 322$), at the surface, it is now the high velocity, small size Ierapetra which dominates. The correction to the larger Mersa Matruh Gyre is smaller, especially in ψ. For the subbasin-scale Rhodes Gyre and Mid-Mediterranean Jet, nonlinear terms only have a small impact. At 500 m depth, the two Straits and Rhodes basin still dominate internal deviations but Case 3 also estimates that the Ierapetra and an anticyclone of the Mersa Matruh-Shikmona Gyre (MM-S-G) complex are above average. For these deep mesoscale vortices, nonlinear terms matter at depth. In Case 4 (nonlinear momentum, $p = 400$), results as these of Case 3, except that standard deviations are a bit larger, to first order by about 6.6% to 7.6% (13.2/2 to 13.2/2/0.868, see footnote 4).

Two general remarks can be made: (i) for accurate flow variability variances, not only the background density field, but also the regional topography, nonlinear and diffusion terms should be considered; (ii) even though subspaces are used, the present global estimates of mesoscale variances are in accord with and complement previous local estimates (e.g. Özsoy *et al.*, 1993; Robinson and Golnaraghi, 1993).

4.2.b A priori mesoscale error eigenvectors and spectrum

Case 2. Figure 10 illustrates the first and second non-dimensional singular vectors, columns of $\mathbf{E}^*$ in (eqs. A21–23). They explain 1.08% and 1.05% of the variance explained by all 322 vectors, respectively. They are examined because several of their properties are representative of those of other dominant vectors. As expected from Sect. 4.2.a, for linear momentum, the variability in early Spring is dominated by large-mesoscale variations of the Rhodes Gyre. In the last decades, the Rhodes Gyre has indeed been observed to be the main subbasin-scale feature of the region (Milliff and Robinson, 1992; Nittis and Lascaratos, 1998).

The first vector (Fig. 10, 1a–b) covers the principal core of the Gyre, above the Rhodes basin. Horizontally (Fig. 10–1a), the main T and S structures are almost axisymmetric, with horizontal decay-scales of about 40 km (radius of 60 km). On the open-ocean side, the main T, S and ψ structures indicate a predominant geostrophic equilibrium. Close to the coastline, this is not true mainly due to decreasing depth and increasing coastal friction. Vertically, T is surface intensified (Fig. 10–1b), with an uniform extremum within 20 to 200 m and a significant extension down to 900–1000 m above the Rhodes basin. The S structure has a subsurface extremum within 250 m to 320 m and a zero-crossing near 100 m. The signs of T and S reverse at about 1500 m and 1300 m, respectively. Below, local extrema are much smaller than the global upper-thermocline extrema. Overall, where T and S are both relatively large, they are in phase, compensating each other in density. The surface $\widehat{u}$ (Fig. 10–1a) and cross-sections in $\widehat{u}$ and $\widehat{v}$ (Fig. 10–1b) confirm a predominant geostrophic equilibrium. A weak topographic wave pattern is also visible in the $\widehat{u}$ map and sub-surface tracer cross-sections. Its average amplitudes are about 20% of those of the main lobes. Vertically, $\widehat{u}$ and $\widehat{v}$ reverse sign near 700 m. The extrema below are 10 times smaller than the surface ones. Using ψ (Fig. 10–1a), a minimum total velocity is expected near 900 m.

The second vector (Fig. 10, 2a–b) mainly relates to displacements of the core of the Gyre, along the north-south axis of the Rhodes basin. Except for the main double lobes in T, S

and ψ, and corresponding triple lobes in $\widehat{u}$ and $\widehat{v}$, most properties are as those of the first vector. Nonetheless, such a displacement of the Gyre's core is logically suggested to interact more with topographic wave patterns (e.g. Smith, 1983) than in the first vector. Along the northern escarpment, the dominant wavelength of the pattern (Fig. 10, 2a–b) is about 160 km (scale of 25 km). Possible wave types and time scales are discussed below.

Other dominant vectors also relate to main features (Fig. 1 and Table 3). This is because to explain a natural variation, a group of vectors is usually required. Considering for example vectors 3 to 16, their largest amplitudes assign the vectors: (3–7,9,12–16) to the Rhodes Gyre; (3–6,13–14) to wave patterns along the northern escarpment and Mid-Mediterranean Ridge; (5–9,11–16) to the Ierapetra; (12–14) to the Mersa Matruh Gyre; (8–16) to the Mid-Mediterranean Jet; (3–4,6,9–16) to the West Cyprus Gyre; (4,6,9,12–16) to the Asia Minor Current; and (9–10,12–16) to the Mersa Matruh-Shikmona Gyre complex. Since each vector is orthogonal to all more dominant ones and 3D dynamical couplings can be complex, a detailed analysis requires additional computations beyond the present scope. Considering the decay of the error spectrum, the variance is distributed such that the dominant 50, 100 and 200 vectors explain 41.4%, 66.7% and 89.4% of the total variance, respectively.

Case 3. Figure 11 is as Fig. 10, but for nonlinear momentum adjustments (Table 1). In accord with variance results (Table 3), the feature of dominant mesoscale variability is then the Ierapetra. The two vectors shown explain 1.59% and 1.24% of the variance explained by all 322 vectors, respectively. These percentages are larger than in Case 2 because nonlinear terms steepen the start and flatten the upper-middle of the eigenvalue spectrum. The first vector corresponds to the vortex itself, the second to eastward-westward displacements.

In comparison with Case 2, horizontal T and S structures in the first vector (Fig. 11–1a) are, when significant[5], closer to Mexican hats and of lesser width (radius near 50 km, decay-scale of 30 km). Vertically (Fig. 11–1b), T and S are more stretched than in Case 2, as one expects for a ring-like vortex. Even though T remains surface intensified, its uniform extremum is deeper, within 50 to 250 m. This agrees with previous results: e.g. the structure of Levantine warm core eddies (Brenner, 1993) and shallow surface mixed-layer of the Rhodes

[5] The lobes far from the vortex in surface S are mainly due to the truncation and have an insignificant extremum based on $\rho = 0.928$ (Table 2.a). They are excited by radiating nonlinear effects (absent in Case 2, Fig. 10) and can be seen where amplitudes are relatively small.

Gyre (e.g. Malanotte-Rizzoli *et al.*, 1996). The dominant feature in T extends down to about 600 m, main depth of the present Ierapetra, instead of about 1000 m for the Rhodes Gyre (Fig. 10). The S structure has a zero-crossing near 80 m and a subsurface extremum within 250 m to 340 m. The signs in T/S reverse at about 1300 m/1100 m which, as for the small extrema below, is shallower than at the Rhodes Gyre. Overall, T and S are still in phase when both important. The ψ, $\widehat{u}$ and $\widehat{v}$ components (Fig. 11, 1a–b) are less close to geostrophic equilibrium than on Fig. 10. The nonlinear, inertial and viscous terms modify the classic geostrophic antisymmetries of $\widehat{u}$ and $\widehat{v}$ with respect to the x and y axes. The horizontal lobes (Fig. 11–1a) present sharp gradients and are tilted, with their heads wider than their tails. Velocity is maximum near a radius of 30 km. Vertically (Fig. 11–1b), $\widehat{u}$ and $\widehat{v}$ reverse sign near 400 m, indicating a minimum total velocity near 600 m based on ψ (Fig. 11–1a). The $\widehat{u}$ and $\widehat{v}$ extrema below are about 10 percent of the surface ones. The variations of the deep counterflow and corresponding density are thus weak. However, they have a large vertical extent (here 1500 m) and can influence the stability of the Ierapetra, as found by forecast sensitivity studies in LER97 and argued in general by Dewar and Killworth (1995) and Killworth, *et al.* (1997).

Based on the second vector (Fig. 11, 2a–b), displacements of the Ierapetra can excite radiative momentum patterns. Such adjustments correlate most to density variations in thermal-wind balance: note the T and S radiation patterns and horizontal $\widehat{u}$ close to a "45 degree shamrock". However, at all depths, $\widehat{u}$ and $\widehat{v}$ have clear asymmetries and amplitude variations which result from local peculiarities of topography, density, nonlinearities and bottom friction (Sect. 4.2.c). In the vertical, most properties are as those of the first vector.

Since the two dominant vectors are modified, the others also differ, even though most of subspace itself remains unchanged (Table 2.b). Considering again vectors 3 to 16, their largest amplitudes assign the vectors: (3–6,8,14–16) to the Ierapetra; (6–16) to the Rhodes Gyre; (4,5,8) to wave patterns along the northern escarpment and Mid-Mediterranean Ridge; (3–4,7–10,12) to the Mersa Matruh Gyre; (8–12,14–16) to the Mid-Mediterranean Jet; (10–14,16) to the West Cyprus Gyre; (10,12,16) to the Asia Minor Current; and (8–16) to the Mersa Matruh-Shikmona Gyre complex. Overall, the dominant 50, 100 and 200 vectors explain 41.1%, 66.2% and 89.4% of the total variance, respectively. These percentages are close to those of Case 2: the result is that here nonlinear terms impact the dominant vectors of the subspace but don't change much of the overall spectrum.

Case 4. The error subspaces of Cases 3 and 4 were estimated to be similar at 86.8% (Table 2.b). Up to an arbitrary sign, their vectors 1 to 15 are almost identical (vectors of Case 4 are only slightly less noisy). Some differences start to occur by vector 16, mainly in the small mesoscales. The additional vectors 323 to 400 include 3D patterns of relatively large horizontal scales and usually "wiggly" vertical structures, or vice-versa. The decay of the error spectrum is similar to that of Case 3: the 50, 100 and 200 dominant vectors explain 38.4%, 62.7% and 85.2% of the variance explained by all 400 vectors, respectively.

4.2.c Dynamical properties

From the dominant mesoscale vectors and fields obtained, the types and scales of possible wave patterns along the northern escarpment and Mid-Mediterranean Ridge (e.g. Case 2), and the dynamical balance of the Ierapetra (e.g. Cases 3–4) can be investigated. Note that the numbers obtained from Cases 3 and 4 are similar, indicating a robustness of the results.

Wave patterns. Using App. B and Fig. 10, locally for a wave packet along the escarpment, $\rho_0 = 1028$ kg/m^3, $L = 25$ km, D is about 1000 m, H is on Fig. 2c, $f_0 = 8.45\ 10^{-5}\,\mathrm{s}^{-1}$ and $\beta_0 = 1.86\ 10^{-11}\,\mathrm{m}^{-1}\,\mathrm{s}^{-1}$ (for $\theta_0 = 35.5$). Computing a reference $\rho_s(z)$ by horizontal average of the density field, this leads an average N_s within D of about $2.5\ 10^{-3}\,\mathrm{s}^{-1}$, a local $R_D = N_s D/f_0 \simeq 30$ km and $R_{\mathrm{ext}} \simeq 1200$ km. For U, based on the second vector (Fig. 10, Panels 2a–b), the sum of the surface internal and external components yields: $U \simeq (3.9 \times 1.5\ 10^{-2} + 5.6\ 10^{7} \times 0.5\ 10^{-2}/H/L)\sqrt{1893} \simeq 3\,\mathrm{cm\,s}^{-1}$ ($1.5\ 10^{-2}$ and $0.5\ 10^{-2}$ are the non-dimensional amplitudes, 3.9 and $5.6\ 10^7$ the normalization factors, and 1893 the eigenvalue). With contributions from other relevant vectors, the characteristic velocity U for a wave packet is about $5\,\mathrm{cm\,s}^{-1}$. Hence, the local non-dimensional numbers are: $Ro = 0.015$, $Bu_{\mathrm{ext}} = 2\ 10^3$, $Bu = 1.4$, $\beta = 0.23$, $\alpha \simeq 25$ and $s \simeq 0.6$ (excepted just east of the island of Rhodes where α and s reach 50 and 1, respectively). The small Ro and large Bu_{ext} indicate that the rigid-lid linear PE regime is appropriate. From β, the planetary vorticity gradient is relatively small and from $\alpha \gg 1$, the topographic vorticity gradient is large: β_0 can be neglected compared to $|\nabla_h H|\frac{f_0}{D}$. From $Bu \sim 1$, the length-scales of the horizontal flow and internal stretching (stratification's strength) match. Since s is close to one, quasi-geostrophy may not apply. Finally, for the model topography (Fig. 2c), s and α are relatively uniform along the escarpment waveguide (about 60 km wide). Based on these numbers and interpretations, the topographic wave packets are

of the coastal-trapped type (Huthnance, 1992; Pedlosky, 1987; Brink, 1991). Note that here, wave patterns arise during rigid-lid momentum adjustments (fixed tracer disturbances): for the barotropic mode along the escarpment, to first-order in s, the frequency is then of the order $\frac{|\nabla_h H| f_0/D}{k}$, where $k = 1/L$ is the wave number. This leads a period of about 1.45 days, i.e. of the order of 1 to 2 days.

In the ocean, wave packets would be generated by complete dynamical adjustments, and also by winds, atmospheric pressure and coastal flows. A complex wave spectrum around the above values can be expected. First, the natural topography is more jagged and at several locations steeper than the model topography, which we estimate could shift the period by about 50%. Second, several wave types are possible along the escarpment and/or Mid-Mediterranean Ridge: in addition to a suite of coastal-trapped waves (e.g. Leblond and Mysak, 1971) like Kelvin and continental shelf waves, inertial and Rossby waves can be generated. For complete statements on scales, shapes and forcings, additional studies are necessary (e.g. Huthnance, 1978; Holland and Webster, 1994). The dominance of such wave patterns and associated mesoscale variations in the vectors related to the Rhodes Gyre (Sect. 4.2.b) suggests that they could be in part responsible for the observed multiple centers of the Gyre (Milliff and Robinson, 1992). In particular, the main core of the Gyre is not stationary, but undergoes translations and precessions of synoptic time-scales (seen in our simulations).

Ierapetra. Using Fig. 11 and local scale analysis, an approximate dynamical balance for the Ierapetra can be obtained. One has $\rho_0 = 1028$ kg/m^3, $L = 20$ km, $D = 400$ m, $H \simeq 2500$ m (Fig. 2c), $f_0 = 8.15\ 10^{-5}\,\mathrm{s}^{-1}$ and $\beta_0 = 1.89\ 10^{-11}\,\mathrm{m}^{-1}\,\mathrm{s}^{-1}$ (for $\theta_0 = 34.1$). The vertical averages within D of N_s and of the horizontal $\Delta\rho$ are $2.5\ 10^{-3}\,\mathrm{s}^{-1}$ and 0.15 kg/m^3, respectively. Hence, $R_D = 12$ km and $R_{\mathrm{ext}} = 770$ km. From Table 3, the mesoscale component of the total surface U is 25 cm s^{-1}. Adding the subbasin-scale component (Sect. 4.1) yields $U \simeq 45$ cm s^{-1}. Hence, for the Ierapetra, relevant non-dimensional numbers are: $Ro = 0.28$, $Bu_{\mathrm{ext}} = 1500$, $Bu = 0.38$, $\beta = 0.017$, $\alpha = 1.8$ and $s = 0.5$. The size of Ro attests that nonlinearities are important while β and Bu_{ext} confirm that the planetary vorticity and stretching of the free-surface do not matter. The above numbers suggest that the dominant horizontal momentum balance within the vertical extent D is the gradient-wind balance: solving for U in, $\frac{U^2}{L} - f_0 U + \frac{\Delta\rho\, g D}{\rho_0\, L} \simeq 0$, gives a root $U \simeq 50$ cm s^{-1} (accounting for the uncertainty in characteristic scales, this root lies between 40 and 70 cm s^{-1}). In the vertical, since Ro and Bu are of the same

order, W is large enough for the vertical convergence and horizontal divergence to balance ($W \simeq UD/L$) and the horizontal changes in density to match the vertical ones ($\Delta\rho \simeq \Delta\rho_s$). Based on α and s, the local topographic valley (Fig. 2c) is a factor in maintaining the location of the vortex. Finally, viscous terms are only important in the bottom layers and at the sub-mesoscales: e.g. the horizontal momentum Ekman number $Ek_h = A_h/f_0L^2$ is 0.92 for scales under 20 km but decays to 5 10^{-4} at 50 km and is almost null beyond 100 km (A_h is the effective Laplacian horizontal eddy viscosity which is here scale-dependent).

4.2.d A priori mesoscale error covariance functions

The covariance function between the surface (5 m) temperature at (33.80N,27.85E: about 80 km east-southeast of the Ierapetra) and the other state variables is chosen as an example. The plots (Figs. 12–13) correspond to elements of a row of $\mathbf{B}^p$ (size $218943 \times p$).

Case 2. Figure 12 shows that the horizontal T–T and T–S Mexican hat covariances are well represented. Vertically (Panel b), the characteristics of tracer covariances are: T–T and T–S uniform within a 30 m surface mixed-layer; subsurface extremum in T–S near 300 m; T–T and T–S positive down to about 1200 m where they change sign; etc. For T–ψ (Panel a), quasi-geostrophic balance is locally a good approximation. However, the horizontal T–$\widehat{u}$ and T–$\widehat{v}$ are not exactly antisymmetric, geostrophic double-lobe structures. At the surface, the main reason is that inertial terms matter at (33.80N,27.85E). If only the inertial and geostrophic terms were important, after 2 days of adjustment integration, with $2\pi/f \simeq 0.89$ days, the T–$\widehat{u}$ pattern at 5 m would be tilted clockwise by almost 45 degrees. With horizontal, vertical and bottom diffusion, this tilt at 5 m is here reduced to about 30 degrees (Panel a). Note that even though inertial oscillations occur (e.g. in numerical simulations, the Ierapetra at the surface rotates in small circles at frequencies close to f), their effects on covariances are not always desired[6]. In the vertical (Panel b), T–$\widehat{u}$ and T–$\widehat{v}$ have a zero-crossing within 500 to 600 m. From T–ψ, total velocity covariances near (33.80N,27.85E) have a vertical minimum near 700 m. Below the zero-crossings, T–$\widehat{u}$ and T–$\widehat{v}$ are opposite to their surface structures, but as in Sect. 4.2.b, amplitudes are much smaller (at most 10% of surface values).

[6] Undesired effects of inertial oscillations arising in adjustments can be made insignificant by allowing the duration of adjustment integrations to be random within an inertial period. This would be useful inside the Rhodes Gyre where nonlinear terms are weak: the tilt in the 5 m T–$\widehat{u}$ and T–$\widehat{v}$ covariances there mainly depends on the duration of adjustment, due to inertial rotations. However, at the Ierapetra where nonlinear terms dominate, the duration of adjustment did not influence the tilt in velocity covariances (the tilt is desired).

Cases 3 and 4. By construction, the tracer auto-covariance functions of Cases 3 and 2 (Fig. 12) are equal. Those of Case 4 are very similar; the main difference is a volume-averaged increase in variance of $100 \times (72 - 67.2)/67.2 = 7.1\%$ (Sect. 4.2), which is distributed in the 3D T–T and T–S fields according to the tracer vectors 323 to 400. Figure 13 thus only illustrates cross-covariances with velocities. Comparing Cases 2 (Fig. 12) and 3 (Fig. 13a), overall, nonlinear momentum adjustment modifies structures, but amplitudes remain similar. Focusing on differences, the horizontal T–$\widehat{u}$ structure has a smaller tilt, of about 15-to-20 degrees clockwise: the nonlinear terms dissipate some inertial oscillations. Cross-covariances now extend to the Ierapetra and their gradients are tighter due to nonlinearities. The T–ψ structure has become asymmetric, with cyclonic T–ψ correlations at the Ierapetra. In the vertical, structures in the upper-layers extend deeper. Other vertical changes are mainly due to the lesser 15-to-20 degree rotation in the horizontal. Considering the velocity cross-covariances of Cases 3 (Fig. 13a) and 4 (Fig. 13b), shape and amplitude differences are small. This agrees with the corresponding global similarity coefficient (Table 2.b).

4.3 Mesoscale: *a posteriori* PE fields

At the mesoscale stage ($w = 2$), the mapping procedures are as overviewed in Sect. 4.1. The differences lie in the *a priori* states (the subbasin-scale estimates), data set and mesoscale covariances (Sect. 4.2). The focus next is on Cases 2 and 3 for the effects of nonlinear momentum terms, and on Cases 3 and 4 for the effects of the size of the subspace.

Tracer fields. Figure 14 illustrates the T, S components of $\mathbf{x}^{\mathrm{a}}$ obtained by multivariate 3D analysis (App. A.3) in the Case 2. By construction, the tracer fields for Case 3 (not shown) are identical. Comparing Cases 2 (Fig. 14) and 4 (Fig. 10 in LAL00), their tracer fields have small differences, in accord with the 4.8% (67.2% to 72%) increase in the 3D tracer variance explained. Differences are largest in the surface layers and small mesoscales, which is the main variability spanned by the additional vectors 323 to 400 used in Case 4. In comparison with Case 1 (Figs. 9 in LAL00), results are analogous to these of Sect. 3. The large mesoscales to the subbasin-scales have small differences, within data error bounds. The sub-mesoscales to small mesoscales present larger differences, especially near the surface. This is because many of these small scales are environmental noise for the available data resolution (Fig. 9a) and because the 400 eigenvectors only explain 72% of the total tracer variance (Sect. 4.2).

Transport fields. Figure 15a is the result of Case 1 which computes ψ by vertically averaging the total velocities in thermal-wind balance with the horizontal T and S analyses, assuming a level of no motion at 600 m. Fig. 15b is the ψ component of $\mathbf{x}^{\mathrm{a}}$ for Case 2: the transport is then globally estimated from the T and S data (Fig. 9) using App. A.3. Fig. 15c is ψ for Case 3, Fig. 15d ψ for Case 4. The advantages of Cases 2–4 (Fig. 15b–d) are that their ψ estimates, and corresponding uncertainties (Sect. 4.4), are in accord with the dominant SVD of PE adjusted perturbations. Most of the regional dynamical features can be distinguished in these ψ fields, but not in those of Case 1. Comparing Fig. 15b and 15c, the effects of nonlinear terms in the momentum adjustments agree with local mesoscale standard deviations (Table 3). Differences are largest for the Ierapetra and Mersa Matruh Gyre. Comparing Fig. 15c and 15d, increasing the size of the subspace leads to small 2 to 10% variations in ψ, in accord with the global covariance similarity of 86.8% (Table 2.b). Largest changes are at the Ierapetra, above the Rhodes basin and along the Asia Minor Current and Mid-Mediterranean Jet.

Internal velocity fields. Figure 16a is the result of Case 1 which computes $\widehat{u}, \widehat{v}$ by thermal-wind balance. Fig. 16b are the surface $\widehat{u}, \widehat{v}$ components of $\mathbf{x}^{\mathrm{a}}$ for Case 2: $\widehat{u}, \widehat{v}$ are then globally estimated from the T and S data (Fig. 9) using App. A.3. Fig. 16c is the same, but for Case 3; Fig. 16d is for Case 4. Differences between Cases 1 and 2 are small and mainly due to their different tracer fields. Nonlinear momentum terms (Cases 2 to 3) mainly affect the Ierapetra and Mersa Matruh Gyre. For the Ierapetra, gradient-wind balance (Sect. 4.2.c) is a good approximation but geostrophy is not. Increasing the size of the subspace (Cases 3 to 4) leads to variations in the small mesoscales, in accord with the variability spanned by the additional vectors considered. Overall, the regional increases in speed from Cases 2 to 3, and from Cases 3 to 4, agree with the *a priori* standard deviations of Table 3 and global values obtained from Table 2.b.

4.4 Mesoscale: *a posteriori* error covariance

4.4.a A posteriori mesoscale error variance

Univariate 2D benchmark. *A posteriori* tracer error variances result from the 2D analyses, e.g. 5 m errors on Fig. 9b. Velocity error variances are set assuming geostrophic balance.

Multivariate 3D scheme. Figures 17a–b illustrate *a posteriori* error standard deviations for Cases 2 and 3 (for Case 4, see Fig. 13 of LAL00). An important result is that error properties

are as one expects dynamically even though only 322 or 400 vectors are used. The tracer errors of Cases 2–4 are similar to these of Case 1 (Fig. 9b). Differences are only due to the use in Cases 2–4 of *a priori* T and S covariances with non-zero multivariate and vertical correlations. By construction, tracer errors for Cases 2 and 3 are identical (up to machine precision).

In general, the structures of velocity errors (Figs. 17a–b) differ from these of tracer errors which mimic the patterns of hydrographic ship-tracks. Differences in shape are much larger for $\widehat{u},\widehat{v}$ errors (under geostrophic influence) than for ψ errors (under hydrostatic influence). The relationships among velocity error patterns, regional dynamical features, and data horizontal and vertical resolutions (un-sampled regions, distances between ship-tracks, spacings between profiles along ship-tracks, non-uniform profile lengths, etc) are discussed in Sect. 5.b.ii of LAL00. These discussions apply here. Focusing on sensitivities, velocity errors for Cases 2–4 differ from these of Case 1 (not shown) because, in Cases 2–4, *a priori* error covariances involving velocities are non-homogeneous and anisotropic in 3D and because the dominant momentum balance is not everywhere geostrophy (diffusion and nonlinearities matter locally). Comparing Cases 2 (Fig. 17a) and 3 (Fig. 17b), the nonlinear momentum terms impact *a posteriori* errors in ψ, $\widehat{u}$ and $\widehat{v}$ at various depths and locations. Differences are largest near the Ierapetra, Mersa Matruh Gyre and Mersa Matruh-Shikmona Gyre complex which we found to be the most nonlinear features *a priori* (Sect. 4.2). Due to nonlinear mixing, error patterns in Case 3 are broader and more uniform (less dependent on data location) than in the linear Case 2. The local variations at depths (see LLA98) among Cases 2–3–4 are in accord with global dissimilarities (Table 2.b) and differences in *a priori* error fields (Sec. 4.2.a).

4.4.b A posteriori mesoscale error eigenvectors and spectrum

The first and second non-dimensional *a posteriori* error singular vectors for Cases 2 and 3 are illustrated on Figs. 18 and 19, respectively (for Case 4, see Fig. 14 of LAL00). For each of Cases 2–4, the data $\mathbf{y}^o$ have redistributed the variance in the subspace. Dominant *a posteriori* vectors have little in common with *a priori* ones. In the linear Case 2 (Fig. 18), the two dominant vectors are associated with the low data resolution along 30.75E (Fig. 9a) and lack of data in the northeast corner (north of 35.5N, east of 29.5E). In Cases 3 (Fig. 19) and 4, this holds for the first vector, but not for the second. The second vector then corresponds to low data resolution patches centered on 29E, which is across the Mersa Matruh-Shikmona

Gyres where nonlinearities matter (Sect. 4.2). In Case 2, the first vector accounts for 5.7% of the normalized *a posteriori* error variance; the second for 5.1%. In Case 3, these numbers are smaller, 5.2% and 4.8%, because some additional kinetic energy due to nonlinear terms remains un-measured in the *a posteriori* eigenvalue spectrum. In Case 4, these numbers further reduce to 4.25% and 4.05% due to the larger subspace size. Overall, eigenvalue spectra differ for the same reasons, but by smaller amplitudes. In Case 2, the dominant 50 vectors explain 75.8% of the variance explained by all 322 vectors; the dominant 100 explain 87.2%. In Case 3, these numbers remain nearly unchanged, 75.5% and 87.2%. In Case 4, they are logically slightly smaller: 71.5% for 50 vectors and 84.5% for 100 vectors out of all 400 vectors. For all Cases, in comparison to *a priori* values (Sect. 4.2.b), the analysis has here steepened the top and flattened the middle and end of the error spectrum.

Structure-wise, Cases 2–4 have almost the same first vector (Figs. 18–19, Panels 1). Due to the nonlinear adjustments, other vectors are reordered in Cases 3–4: e.g. up to effects of the orthogonality constraint and arbitrary sign, the second vector of Case 2 is as the third of Case 3 (not shown) and inversely (Fig. 19). However, the dominant vectors of Cases 3 and 4 are almost identical, indicating a convergence. Locally, both dynamics and data affect all vectors. Focusing here on data coverage (see LAL00 for dynamical effects), consider for example the first vector of Cases 2–4 (Figs. 18–19, Panels 1a–b). For each variable, amplitudes north of 35.5N in the corner without data are at least twice as large as they are south of 35.5N. The zero-crossings (maxima) of the T and S patterns of this first vector are also aligned with the (lack of) meridional ship-transects (Fig. 9): from 34N to 35.5N included, zero-crossings are every 0.5 degrees of latitude, while north of 35.5N, the last lobe covers 0.8 degrees of latitude, across the no-data corner. Profile depths also influence error patterns. For example, east of 30.25E, all profiles are about 1000 m deep, except for two at (31E,35.5N) and (31E,34.5N) which are 2000 m deep. Logically, these two deep profiles reduce the error on $\widehat{u}$ at 35N but not on $\widehat{v}$ (see Panels 1b from 1000 to 2000 m). Analogous facts hold for other vectors.

4.4.c A posteriori mesoscale error covariance functions

Comparing *a priori* (Figs. 12–13, Sect. 4.2.d) and *a posteriori* (Figs. 20–21) error covariance functions also shows data impacts. All amplitudes are reduced in accord with the data coverage and measurement error model (App. A). At (33.80N,27.85E), both the horizontal and vertical correlation scales have been reduced to small mesoscale values.

Case 2. Horizontal structures (Fig. 20a) clearly show the influences of the low data resolution south of 34N within 28–29E and of the three ship-tracks along 26E, 26.5E and 27E (Fig. 9a). In the vertical, T–T and T–S structures have stronger negative lobes and are more surface intensified because *a priori* T and S data errors are modeled to decay with depths (Fig. 23 in Sect. 5.2). The T–$\widehat{u}$ and T–$\widehat{v}$ structures have remained similar and surface intensified, but the negative lobe of T–$\widehat{u}$ is now to the east, in accord with thermal-wind effects and lower data resolution in that direction.

Cases 3 and 4. Only Case 4 is shown (Fig. 21). Case 3 is analogous, up to amplitudes which are smaller in accord with the global similarity coefficient (Table 2.b). In the horizontal (Fig. 21a), structures in Case 4 are similar to these in Case 2 (Fig. 20a), except that gradients are tighter due to nonlinearities and larger subspace size. In cross-covariances with velocities, differences are largest where features have been shown to be most nonlinear (e.g. Table 3). In the vertical, for all covariances, gradients are tighter than in Case 2. Vertical patterns in T–$\widehat{u}$ and T–$\widehat{v}$ have remained similar, but these of T–T and T–S are more complex, in accord with the additional small mesoscales explained by the vectors 323–400.

5. QUANTITATIVE EVALUATION OF FIELDS AND IMPACT ON FORECAST PERFORMANCE

The two mapping schemes and three error subspaces (Cases 2–4) are now evaluated by measuring the skill of forecasts initialized from the four analyses on March 27 (Cases 1–4). Note that for analyses centered on other dates (not shown), results are analogous. Starting from each gridded state (e.g. Figs. 14–16), the numerical PE model is first integrated forward in time. Forecasts are then compared to *in situ* hydrographic data and satellite sea surface temperature (SST) data. Due to the interactions between tracers and velocities, the effects of the initial flow fields and velocity error subspaces are also assessed.

During March 26–April 8, *in situ* samplings are relatively intensive (see Fig. 23a below) and the corresponding CTD profiles are used to evaluate forecasts. The high-resolution satellite images (GISIS, 1995) are interpolated onto the numerical model grid, masking cloudy areas. During March 27–April 3, on three days, different halves of the grid are clear and contain limited noise (e.g. Fig. 22a). This leads to a relatively good week-composite, even though one should beware of non-synoptic patching (LLA98). These interpolated day and week images are used to evaluate forecasts.

An issue is that the interval during which forecasts can be compared is limited by the predictive capability of the prediction system. Beyond this limit, nonlinear integrations of data and model errors could reverse conclusions. For the area, period, regime of interest and data available, the present limit is near 10 days (LER97). Forecasts are thus not compared beyond that. Remaining issues are to define the error and choose its measure. Since comparing forecasts to analyses of data can be misleading, data and forecasts are here directly compared at data points. These data-forecast residuals can be a good estimate of forecast error, in so far as they are larger than the errors in the data. They are measured by root-mean-squares (RMS), correlation coefficients and pattern correlation coefficients (PCC).

5.1 Satellite SST data

Considering first daily images (e.g. Fig. 22), it is challenging to determine qualitatively which of the forecasts is closest to the satellite SST. Quantitatively, their global scores are indeed similar (see Table 4 below). Focusing on differences, overall, gradients are more accurate in the multivariate 3D scheme (Cases 2–4) than in the benchmark (Case 1). The branch of the Mid-Mediterranean Jet near 33N (on Fig. 22a, seen starting at 29E) is also better represented in Cases 2–4 (Figs. 22c,d,e). The lobes of the Mersa Matruh Gyre are visible in Cases 1 and 4 (Figs. 22b,e), but not so much in the Cases with the smaller subspace size (Figs. 22c,d). For the Ierapetra and its surrounding cold vortices, Cases 1 and 4 have similar large mesoscales. At the small mesoscales, Cases 1 and 4 are better than Cases 2 and 3; overall, the Ierapetra gradients of Case 4 are the most accurate. Comparable comments hold for other daily images (not shown). Considering the week composite (Fig. 30 in LLA98), similar statements can again be made, including for the Rhodes Gyre.

In Table 4, the skill of forecasts generated from the different analyses is evaluated quantitatively. For the three relatively clear days, the correlation coefficient between the satellite SST day composite and estimated 5 m temperature for that day is given (Table 4a). To obtain these coefficients, the horizontal mean of each field is removed first. In Table 4b, the week composite is compared with the week average of the day-to-day 5 m temperature forecasts. To take advantage of the larger composite coverage, two more measures are evaluated: (i) the RMS of the residuals between the clear satellite data and averaged forecasts, and (ii), the PCC defined by, $\mathrm{PCC} \doteq \frac{(\mathbf{T}^S - \mathbf{T}^b)^T (\widehat{\mathbf{T}} - \mathbf{T}^b)}{||\mathbf{T}^S - \mathbf{T}^b||_2 \; ||\widehat{\mathbf{T}} - \mathbf{T}^b||_2}$, where the vector $\mathbf{T}^S$ is the satellite week composite, $\widehat{\mathbf{T}}$

the estimated week average and $\mathbf{T}^b$ the background set to the satellite month composite for March 1995. In all computations, only common cloud-free points are considered.

Table 4. Day and week measures of skill for temperature: satellite SST vs. estimated T fields at 5 m

a. *Day Cor. Coef.* Day composite vs.	Case	March 27 Nowcast	March 28 1-day forecast	April 3 7-day forecast
	1	0.57	0.76	0.82
	2	0.67	0.77	0.81
	3	0.67	0.76	0.81
	4	0.66	0.76	0.81
b. *Week measures*	Case	Cor. Coef.	PCC	RMS Diff.
(March 27–April 3	1	0.76	0.18	0.3912
week composite vs.	2	0.75	0.20	0.3894
average of eight	3	0.75	0.21	0.3870
estimated T fields)	4	0.76	0.20	0.3895

For the day snapshots (Table 4a), the main difference is on March 27: the nowcasts of Cases 2–4 are about 15% better than that of the univariate 2D Case 1. On other days, a surprising result is that there is little variation among Cases. This is mainly due to uncertainties in the satellite data, even though it also reflects the subspace convergence. Another artifact of data errors and also varying data coverage is the increasing correlation with time. For the week composite (Table 4b), correlation coefficients are analogous. The PCCs indicate that Case 1 is the worst and Case 3 the best (adding more vectors can thus at times decrease performance). These PCC numbers are relatively low. This is mainly because they focus on the small mesoscale for which the PCC skill is smaller than for the large mesoscale and subbasin-scale due to the initial data resolution. The RMSs indicate an error slightly larger for Case 1 than for Cases 2–4, but variations are not significant (the estimated error in the *in situ* data at the surface is around 0.3°C, see Fig. 23 below). For the day images, the RMS and PCC (not given) lead to the same conclusions. Overall, the satellite data indicate that the skills of Cases 2–4 are similar and only a few times slightly larger than the skill of Case 1.

5.2 *In situ* data

In the evaluations based on *in situ* T and S data (Fig. 23a), time is divided in periods of three days. For each of these periods, data-forecast residuals are computed at the intersections of the CTDs with the model grid, using the forecast for the center of the period (measurement model details are in LER97). These residuals are measured by RMS, averaging level by level. On Fig. 23b, the resulting RMS-error (RMSE) estimates are plotted for the temperature and

salinity of Cases 1 and 4, on 12 horizontal model levels (from 0 to 500 m depth). Overall, forecast errors increase with forecast durations and decrease with depths in proportion to the variability. For March 26–28 (Rhodes Gyre area) and March 29–April 1 (near 30E), most RMSEs are below the estimated error standard deviations of the data. Both schemes likely lead to good forecasts. Focusing where RMSEs are significant, Case 4 is better than Case 1 at the surface, but the opposite holds near 500 m. For April 3–5 (data along the Cretan Arc), RMSEs are much larger, in accord with the longer forecast duration and also lesser quality of the numerical model in this region. For T, Case 1 is better than Case 4 at all depths. For S, Case 4 is substantially better than Case 1 in the surface layers, but is worse below. For April 6–8, at the surface, Case 4 is better for T, but not for S. At mid-depths, the situation reverses. Near 500 m, Case 1 is best but errors become smaller than the estimated data error.

These results first confirm that the two schemes have similar skill. They also restate that the univariate 2D scheme can be too sensitive to small scale noise (e.g. Sect. 3.2), hence the usually lesser skill in the surface layers. They show that the present multivariate 3D scheme can sometimes be less effective at depth. To improve this, either the subspace can be enlarged or the specification of the initial covariance decomposition (Apps. A.1–2) refined. For example, in coastal regions, the lack of better performance at depth is likely due to the initial tracer covariances which were simplified (e.g. horizontally homogeneous, vertically dominated by open-ocean data structures instead of coastal ones).

6. SUMMARY AND CONCLUSIONS

The foregoing study investigated the influence of *a priori* parameters on the error subspace estimation and mapping methodology introduced in (Lermusiaux *et al.*, 2000, henceforth, LAL00). The sensitivities of the subspace and of the *a posteriori* gridded fields and errors to the size of the subspace, scales considered and nonlinearities in the dynamical adjustments were exemplified and studied for mesoscale to subbasin-scale physical fields in the northwestern Levantine during February 10-March 15 and March 19-April 16, 1995. *A posteriori* field and error estimates were evaluated by comparison among each other and by using the univariate 2D analysis scheme of HOPS as a benchmark. Forecasts generated from the various analyses were qualitatively and quantitatively compared to *in situ* and satellite data. A simple back-of-the-envelope rule for the required size of error subspaces was also outlined and utilized.

Several three-dimensional, multivariate and multiscale properties were illustrated. Our global mapping was shown to: estimate simultaneously all physical fields and errors from the tracer data; usefully decompose multivariate covariances; improve vertical correlations and the filtering of environmental noise; yield more accurate field gradients; and, lead to velocities that are close to being PE adjusted and *a posteriori* velocity errors that are PE consistent. In comparison to the geostrophic benchmark, gains from our methodology were largest where topographic, nonlinear and diffusion terms mattered. In particular, *a posteriori* errors were found to reflect complex properties of both the data utilized and regional dynamics (not always close to geostrophic). Based on the forecasts from the various analyses, the multivariate 3D scheme performed as well as the benchmark. Similar conclusions have been drawn in meteorology (Andersson *et al.*, 1998). Presently, this is likely in part due to the limited data.

Based on sensitivities to scales, for a fixed domain size, smaller scales usually require larger subspaces due to spectral redness. Based on sensitivities to the size of the subspace, truncating the *a priori* error covariance to a converged subspace is efficient and *a priori* error eigenvectors of eigenvalues negligible with respect to data errors can be neglected. In the Levantine, increasing the subspace size usually improved the analysis at depths and the small mesoscales. Overall, the variations of *a posteriori* fields with the parameters of the subspace were as indicated by a global similarity coefficient: if *a priori* error covariance matrices differed by about 5% (in the standard deviation sense), so did the fields and *a posteriori* errors. Based on sensitivities to the dynamics of adjustments, it was found however that even when subspaces are globally similar, some of their dominant vectors can be quite different. For example, the nonlinear momentum correction modified the dominant vectors from large-mesoscale variations of the Rhodes Gyre to mesoscale variations of the Ierapetra eddy. It also modified the shape of error spectra, the structures of covariance functions and some properties of the *a posteriori* fields and errors. Relative linear-nonlinear differences were computed and as anticipated found to be largest for the features and regions with high shears, around deep eddies or gyres (e.g. Ierapetra, Mersa Matruh Gyre), along fronts (e.g. Mid-Mediterranean Jet) and in Straits. The impacts of inertial oscillations on the subspace adjustment were also discussed.

The study of *a priori* tracer and velocity variances, spectra of eigenvalues, shapes and amplitudes of dominant multivariate eigenvectors, and structures of (cross)-covariance functions revealed several dynamical properties. The spatial distribution of characteristic hydrographic

and velocity scales as well as dominant dynamical balances were quantitatively obtained for most features of the northwestern Levantine. In particular, the Ierapetra eddy was found to be close to gradient-wind balance in the Spring of 1995. Coastal-trapped waves were also inferred to be likely along the northern escarpment of the basin and to account for a significant portion of the global variations of momentum and density fields in the region.

Focusing on research directions, a first issue relates to data availability and accurate multiscale statistical models. Mainly for fair comparisons with the univariate 2D scheme but also for lack of sufficient data, a successive correction approach was used instead of a general one for multiple interacting scales. *A priori* tracer covariance functions were also assumed homogeneous and isotropic in the horizontal instead of being non-homogeneous and anisotropic in 3D as velocity covariances were. These two assumptions can be removed in principle (LAL00). In regions with more data than here (to allow accurate fits), the performance of the 3D scheme may then be improved. Another direction concerns algorithms for efficient dynamical adjustment of the error subspace. For example, specific models or processes (e.g. free surface, coupled biochemical irreversibilities, stochastic internal waves) may require specific adjustment procedures. Additional convergence criteria (App. A) should also be investigated. For example, our experience in other regions suggest that taking into account each variable separately as well as all variables as a whole (eqs. A22) is useful. In these criteria, ideal normalizations for specific purposes should also be researched. Most results obtained here apply to the analysis step of data assimilation schemes based on error subspaces. Other research opportunities thus include: error forecasting and adaptive sampling (e.g. Lermusiaux, 1999b), model improvements (e.g. LER97), dynamical studies (e.g. Lermusiaux, 2001; Lermusiaux and Robinson, 2001), and interdisciplinary applications (Robinson and Lermusiaux, 2001).

Acknowledgements

I am grateful to Prof. D.G.M. Anderson, Dr. C.J. Lozano and two anonymous referees for constructive comments on the manuscript, and to Prof. A.R. Robinson, Dr. P.J. Haley and Mr. W.G. Leslie for their encouragements. I thank the individuals who participated in the LIW95 experiment, the POEM collaboration sponsored by the IOC of UNESCO, Mr. R. Meisner (DLR) for answering questions on the GISIS filtering of the satellite data and Ms. M. Armstrong for preparing some figures. This work was supported in part by the Office of Naval Research under grants N00014–95–1–0371, -97–1–0239 and -00–1–0771 to Harvard University.

APPENDIX A

A priori error subspace estimation and mapping methodology

Algorithms introduced in LAL00 for the estimation/initialization of 3D multivariate and multiscale geophysical fields and their dominant errors are summarized. The main step is the construction of the dominant *a priori* error covariance. The framework is that of continuous-discrete estimation and Ide *et al.* (1997) is used. The true (superscript $^{\mathrm{t}}$) state vector $\mathbf{x}^{\mathrm{t}} \in \mathrm{R}^n$ is assumed subject to the stochastic dynamical and measurement models, respectively,

$$d\mathbf{x}^{\mathrm{t}} = \mathcal{M}(\mathbf{x}^{\mathrm{t}}, t)\, dt + d\boldsymbol{\eta}^{\mathrm{t}}(t) \ , \tag{A1a}$$

$$\mathbf{y}^{\mathrm{o}} = \mathcal{H}\big(\mathbf{x}^{\mathrm{t}}(t_0)\big) + \boldsymbol{\epsilon} \ , \tag{A1b}$$

where $\mathcal{M}$ is the dynamics operator, $\boldsymbol{\eta}^{\mathrm{t}}$ a random process of zero mean and covariance matrix $\mathbf{Q}$, $\mathbf{y}^{\mathrm{o}} \in \mathrm{R}^m$ the data vector, $\mathcal{H}$ the measurement operator and $\boldsymbol{\epsilon}$ a random process of zero mean and covariance matrix $\mathbf{R}$. The time t_0 for the estimation is fixed and $\mathbf{R}$ includes a term for data decorrelation with time (see footnote 2 and LER97). An unbiased estimate of $\mathbf{x}^{\mathrm{t}}(t_0)$ is denoted by $\mathbf{x} \in \mathrm{R}^n$. The state error covariance is defined by $\mathbf{P} \doteq \mathcal{E}\big\{\big(\mathbf{x} - \mathbf{x}^{\mathrm{t}}(t_0)\big)\big(\mathbf{x} - \mathbf{x}^{\mathrm{t}}(t_0)\big)^T\big\} \in \mathrm{R}^{n\times n}$, where $\mathcal{E}\{\cdot\}$ is the statistical mean operator. For the present minimum error variance criterion (Sect. 1), an error subspace of dimension p is the portion of R^n which is spanned by the eigenvectors corresponding to the dominant p eigenvalues of a (normalized) error covariance. With this rational reduction, the optimal estimate becomes:

$$\left\{ \mathbf{x}^{\mathrm{a}} \;\middle|\; \min_{\mathbf{x}} \ \mathrm{tr}\,[\mathbf{P}^{\mathrm{a}^p}]\,, \ \text{knowing } [\mathbf{y}^{\mathrm{o}}, \mathbf{R}] \text{ and } \left[\mathbf{x}^{\mathrm{b}}, \mathbf{P}^{\mathrm{b}^p}\right] \right\} \ , \tag{A1c}$$

in which $\mathbf{x}^{\mathrm{t}}(t_0)$ is subject to (A1a–b). The superscripts $(^{\mathrm{b}})$ and $(^{\mathrm{a}})$ refer to estimates before mapping (*a priori*) and after mapping (*a posteriori*). The superscript $(^p)$ indicates a rank-p approximation: e.g. the *a priori*/*a posteriori* principal error covariance $\mathbf{P}^{\mathrm{b}^p}/\mathbf{P}^{\mathrm{a}^p}$ is the rank-p eigendecomposition of $\mathbf{P}^{\mathrm{b}}/\mathbf{P}^{\mathrm{a}}$. Quantities marked with asterisks are normalized.

A.1 Observed portions of the *a priori* error covariance

The value of a field ϕ at location $(\mathbf{r}, z)$, where $\mathbf{r} = (x, y)$ and z are horizontal and vertical positions in a suitable coordinate system, is denoted by $\phi(\mathbf{r}, z)$. The *a priori* error covariance function for the fields $\phi(\mathbf{r}_1, z_1)$ and $\varphi(\mathbf{r}_2, z_2)$ is then,

$$C_{\phi\varphi}(\mathbf{r}_1, \mathbf{r}_2, z_1, z_2) \doteq \mathcal{E}\left\{ \big(\phi^{\mathrm{b}}(\mathbf{r}_1, z_1) - \phi^{\mathrm{t}}(\mathbf{r}_1, z_1)\big)\big(\varphi^{\mathrm{b}}(\mathbf{r}_2, z_2) - \varphi^{\mathrm{t}}(\mathbf{r}_2, z_2)\big) \right\} \ . \tag{A2}$$

An often efficient representation of (A2) is obtained by expanding the *a priori* errors into,

$$\phi^{\mathrm{b}}(\mathbf{r},z) - \phi^{\mathrm{t}}(\mathbf{r},z) = \sum_{i=0}^{\infty} \phi_i(\mathbf{r})\ Z^*_{\phi_i}(z)\ , \tag{A3a}$$

$$\varphi^{\mathrm{b}}(\mathbf{r},z) - \varphi^{\mathrm{t}}(\mathbf{r},z) = \sum_{i=0}^{\infty} \varphi_i(\mathbf{r})\ Z^*_{\varphi_i}(z)\ , \tag{A3b}$$

where the $Z^*_{\phi_i}(z)$'s and $Z^*_{\varphi_i}(z)$'s are vertical functions, normalized in some suitable sense. Substituting (A3a–b) into (A2) yields,

$$C_{\phi\varphi}(\mathbf{r}_1,\mathbf{r}_2,z_1,z_2) = \sum_{i,j=0}^{\infty,\infty} A_{\phi_i,\varphi_j}\ C^*_{\phi_i,\varphi_j}(\mathbf{r}_1,\mathbf{r}_2)\ Z^*_{\phi_i}(z_1)\ Z^*_{\varphi_j}(z_2)\ , \tag{A4a}$$

where the factor $A_{\phi_i,\varphi_j} = A_{\varphi_j,\phi_i}$ is the horizontal average of $\mathcal{E}\{\phi_i(\mathbf{r})\varphi_j(\mathbf{r})\}$ and $C^*_{\phi_i,\varphi_j}(\mathbf{r}_1,\mathbf{r}_2)$ $\doteq \mathcal{E}\{\phi_i(\mathbf{r}_1)\varphi_j(\mathbf{r}_2)\}^*$ the non-dimensional horizontal cross-covariance function associated with ϕ_i and φ_j. The representation (A4a) is efficient if

$$C_{\phi\varphi}(\mathbf{r}_1,\mathbf{r}_2,z_1,z_2) \simeq \sum_{i,j=0}^{I,J} A_{\phi_i,\varphi_j}\ C^*_{\phi_i,\varphi_j}(\mathbf{r}_1,\mathbf{r}_2)\ Z^*_{\phi_i}(z_1)\ Z^*_{\varphi_j}(z_2) \tag{A4b}$$

with small indices I and J (i.e. A_{ϕ_i,φ_j}'s decay rapidly with increasing i and j).

In Sect. 3.c of LAL00, algorithms for estimating the dominant components of error covariance matrices based on the functionals (A4b) are outlined for three types of assumptions involving: a single scale, multiple but independent scales and general multiple scales. In each of these assumptions, the vertical and horizontal decompositions can be obtained either directly from data (EOFs of scale-restricted data residuals) or from an analytical model fit to data (eigendecomposition of a specified covariance matrix).

A.2 Present construction of the *a priori* error subspace

Here, the discrete state vector $\mathbf{x} \doteq (\widehat{\mathbf{u}}, \widehat{\mathbf{v}}, \mathbf{T}, \mathbf{S}, \mathbf{p}) \in \mathrm{R}^n$ contains gridded values of the $\widehat{u}$, $\widehat{v}$, T, S and ψ fields (see footnote 1). The corresponding *a priori* error covariance estimate, $\mathbf{B}$ (superscript $^{\mathrm{b}}$ omitted), is constructed as follows.

Observed portions. For the observed T and S, the assumption of multiple but independent scales is made and (A4b) becomes,

$$C_{\phi\varphi}(\mathbf{r}_1,\mathbf{r}_2,z_1,z_2) \simeq \sum_{w=0}^{2} R^*_{\phi w,\varphi w}(\mathbf{r}_1,\mathbf{r}_2)\, Z_{\phi w,\varphi w}(z_1,z_2)\ , \tag{A5}$$

for ϕ and φ any four combinations of T and S. As in the univariate 2D scheme, for each scale w in (A5), $R^*_{T_wT_w}$, $R^*_{S_wS_w}$ and $R^*_{T_wS_w}$ are also assumed equal. The tracer submatrix $\mathbf{B}_{\rm trc}$ of $\mathbf{B}$ is then the sum of Kronecker products of vertical $\mathbf{C}^z_{{\rm trc}_{\rm w}}$ and horizontal $\mathbf{C}^{\mathbf{r}^*}_{{\rm trc}_{\rm w}}$ covariances,

$$\mathbf{B}_{\rm trc} = \sum_w \mathbf{B}_{{\rm trc}_{\rm w}} = \sum_w \mathbf{C}^z_{{\rm trc}_{\rm w}} \otimes \mathbf{C}^{\mathbf{r}^*}_{{\rm trc}_{\rm w}} \ . \tag{A6}$$

The algorithm used here to construct $\mathbf{B}^p_{{\rm trc}_{\rm w}}$ is outlined in Table A.a (A7–16): for each scale w, $\mathbf{C}^z_{{\rm trc}_{\rm w}}$ is obtained from data (A7–10) and $\mathbf{C}^{\mathbf{r}^*}_{{\rm trc}_{\rm w}}$ from an analytical model fit to data (A11–12). Normalization matrices are denoted by $\mathbf{N}$. They are block-diagonal: for each field, the corresponding element of $\mathbf{N}$ is the sample and spatial averaged variance.

Table A. *A priori* error subspace construction for one scale (w is omitted)

A.a Observed Portions		
Tracer Vertical EOFs		
Compute scale-restricted *a priori* tracer residuals:	$\mathbf{d}_i = \mathbf{y}^{\rm o}_i - \mathcal{H}_i(\mathbf{x}^{\rm b}) \ , \quad i = 1, \ldots, s \ .$	(A7)
Remove horizontal average, normalize:	$\mathbf{d}^*_i = \mathbf{N}_d^{-1}(\mathbf{d}_i - \overline{\mathbf{d}_i}) \ .$	(A8)
Compute SVD of normalized tracer residuals:	$\mathrm{SVD}\left(\mathbf{S}^*_d \doteq \left[\mathbf{d}^*_1, \ldots, \mathbf{d}^*_s\right]\right) = \mathbf{E}^*_d \boldsymbol{\Sigma}^*_d {\mathbf{V}^*_d}^T .$	(A9)
Leads to tracer vertical covariance decomposition:	$\mathbf{C}^z_{\rm trc} = \mathbf{E}^z_{\rm trc} \boldsymbol{\Pi}^z_{\rm trc} {\mathbf{E}^z_{\rm trc}}^T ,$ where $\mathbf{E}^z_{\rm trc} = \mathbf{N}_d \mathbf{E}^*_d$ and $\boldsymbol{\Pi}^z_{\rm trc} = {\boldsymbol{\Sigma}^*_d}^2 / s \ .$	(A10)
Tracer Horizontal Covariance Eigendecomposition		
Specify normalized covariance from analytical fit:	$\mathbf{C}^{\mathbf{r}^*}_{\rm trc}$ filled from $R^*_{\phi,\varphi}(\mathbf{r}_1, \mathbf{r}_2)$ in (A5).	(A11)
Compute SVD or eigendecompose:	$\mathbf{C}^{\mathbf{r}^*}_{\rm trc} = \mathbf{E}^{\mathbf{r}^*}_{\rm trc} \ \boldsymbol{\Pi}^{\mathbf{r}}_{\rm trc} \ {\mathbf{E}^{\mathbf{r}^*}_{\rm trc}}^T .$	(A12)
Tracer 3D Covariance Eigendecomposition		
Based on Kronecker product of (A10) and (A12):	$\mathbf{B}_{\rm trc} = \mathbf{C}^z_{\rm trc} \otimes \mathbf{C}^{\mathbf{r}^*}_{\rm trc} \ .$	(A13)
Sort eigenproducts $\lambda_z \lambda_r$ and truncate to subspace:	p dominant $\lambda_z \lambda_r \Rightarrow$ diagonal $\boldsymbol{\Pi}_{\rm trc} \ .$	(A14)
Construct corresponding 3D eigenvectors:	p dominant $\mathbf{e}_z \otimes \mathbf{e}_r \Rightarrow$ rank-p orthogonal $\mathbf{E}_{\rm trc} \ .$	(A15)
Result is rank-p decomposition for considered scale:	$\mathbf{B}^p_{\rm trc} = \mathbf{E}_{\rm trc} \boldsymbol{\Pi}_{\rm trc} \mathbf{E}^T_{\rm trc} \ .$	(A16)

Complete multivariate formulation. The velocity portions of $\mathbf{B}$ are computed through an ensemble of adjustment momentum integrations. The algorithm for a given scale w is outlined in Table A.b. An ensemble of perturbed tracers $\mathbf{x}^{{\rm b}^j}_{\rm trc} \doteq (\mathbf{T}^{{\rm b}^j}, \mathbf{S}^{{\rm b}^j})$ is created (A17). The corresponding PE adjusted velocities are obtained by momentum integrations (A19), starting from unbalanced, e.g. geostrophic, initial conditions (A18). Adjusted variability samples are then formed (A20), normalized and organized by SVD (A21). New adjustments (A17–21) are carried out to increase p until (A22) determines that the number of samples is large enough. Once this occurs, $\mathbf{B}^p$ is obtained (A23). In (A22), the pairs $(\mathbf{E}^*, \boldsymbol{\Pi} = \frac{1}{p}\boldsymbol{\Sigma}^2)$ of rank p and $(\widetilde{\mathbf{E}}^*, \widetilde{\boldsymbol{\Pi}} = \frac{1}{\tilde{p}}\widetilde{\boldsymbol{\Sigma}}^2)$ of rank $\tilde{p} \leq p$ correspond to "new" and "previous" estimates of $\mathbf{B}^p$: with the weighted inner products, $\widetilde{\boldsymbol{\Pi}}^{\frac{1}{2}} \widetilde{\mathbf{E}}^{*T} \mathbf{E}^* \boldsymbol{\Pi}^{\frac{1}{2}}$, both principal error directions and amplitudes are compared (other criteria are in LER97). In (A23), $\boldsymbol{\Gamma}$ is a scaling, block diagonal matrix.

A.b Complete Primitive Equation Based Formulation

Form ensemble of perturbed *a priori* tracer fields: $\mathbf{x}^{\mathrm{b}j}_{\mathrm{trc}} = \mathbf{x}^{\mathrm{b}}_{\mathrm{trc}} + \mathbf{E}_{\mathrm{trc}} \boldsymbol{\Pi}^{\frac{1}{2}}_{\mathrm{trc}} \mathbf{u}^j \ , \quad j = 1, ..., p \, ,$ (A17)
where here $\mathbf{u}^j = \sqrt{p}\mathbf{e}^j$.

Form ensemble of unbalanced *a priori* state vectors: $\widetilde{\mathbf{x}}^{\mathrm{b}j} \doteq \left(\widehat{\mathbf{u}}^{\mathrm{b}}, \widehat{\mathbf{v}}^{\mathrm{b}}, \mathbf{x}^{\mathrm{b}j}_{\mathrm{trc}}, \mathbf{p}^{\mathrm{b}}\right) ,$ (A18)

Run p dynamical momentum adjustments: Integrate in (A1a) with $\mathbf{x}_0 = \widetilde{\mathbf{x}}^{\mathrm{b}j}$ and here $\mathbf{x}^{\mathrm{b}j}_{\mathrm{trc}}$ fixed to yield adjusted $\mathbf{x}^{\mathrm{b}j}$. (A19)

Form differences of PE adjusted fields, normalize: $\mathbf{S}^{\mathrm{b}} \doteq \left[\mathbf{x}^{\mathrm{b}1} - \mathbf{x}^{\mathrm{b}} \, ; \, \ldots \, ; \, \mathbf{x}^{\mathrm{b}q} - \mathbf{x}^{\mathrm{b}}\right]; \ \mathbf{S}^* = \mathbf{N}^{-1}\mathbf{S}^{\mathrm{b}}.$ (A20)

Compute SVD of rank p: $\mathrm{SVD}_p(\mathbf{S}^{\mathrm{b}}) \doteq \mathbf{N}\,\mathrm{SVD}_p(\mathbf{S}^*) = \mathbf{E}\boldsymbol{\Sigma}\mathbf{V}^T; \ \mathbf{E} = \mathbf{N}\mathbf{E}^*.$ (A21)

Restart (A17–21) and evaluate convergence criterion: $\rho = \dfrac{\sum_{i=1}^{\bar{p}} \sigma_i(\widetilde{\boldsymbol{\Pi}}^{\frac{1}{2}} \widetilde{\mathbf{E}^*}^T \mathbf{E}^* \boldsymbol{\Pi}^{\frac{1}{2}})}{\sum_{i=1}^{p} \sigma_i(\boldsymbol{\Pi})} \ \geq \alpha \, ,$ (A22)
where $\rho \leq 1$, α is a chosen limit $(1 - \epsilon \leq \alpha \leq 1)$ and $\sigma_i(\cdot)$ selects the singular value number i.

Result is principal error covariance estimate: $\mathbf{B}^p = \boldsymbol{\Gamma}\,\mathbf{E}\boldsymbol{\Pi}\,\mathbf{E}^T\boldsymbol{\Gamma}^T \, .$ (A23)

A.3 Error subspace mapping scheme

With $\mathbf{x}^{\mathrm{b}}$, $\mathbf{B}^p$ (A23) and (A1a–b), the extremum of (A1c) yields the *a posteriori* estimates $\mathbf{x}^{\mathrm{a}}$, $\mathbf{E}^{\mathrm{a}}$ and $\boldsymbol{\Pi}^{\mathrm{a}}$, hence $\mathbf{B}^{\mathrm{a}p} \doteq \mathbf{E}^{\mathrm{a}}\boldsymbol{\Pi}^{\mathrm{a}}\mathbf{E}^{\mathrm{a}T}$. For direct inversion, (A1b) is linearized in the vicinity of $\mathbf{x}^{\mathrm{b}}$ and $\mathbf{x}^{\mathrm{a}}$ is hypothesized to be a linear function of $\mathbf{x}^{\mathrm{b}}$ and $\mathbf{y}^{\mathrm{o}} - \mathcal{H}(\mathbf{x}^{\mathrm{b}})$, each of which is assumed unbiased. The extremum is then (LER97),

$$\mathbf{x}^{\mathrm{a}} = \mathbf{x}^{\mathrm{b}} + \mathbf{E}\boldsymbol{\Pi}\mathbf{H}^{pT}\left(\mathbf{H}^p\boldsymbol{\Pi}\mathbf{H}^{pT} + \mathbf{R}\right)^{-1}\left(\mathbf{y}^{\mathrm{o}} - \mathcal{H}(\mathbf{x}^{\mathrm{b}})\right) \, , \tag{A24a}$$

$$\mathbf{U}\boldsymbol{\Pi}^{\mathrm{a}}\mathbf{U}^T = \widetilde{\boldsymbol{\Pi}}^{\mathrm{a}} \doteq \boldsymbol{\Pi} - \boldsymbol{\Pi}\mathbf{H}^{pT}\left(\mathbf{H}^p\boldsymbol{\Pi}\mathbf{H}^{pT} + \mathbf{R}\right)^{-1}\mathbf{H}^p\boldsymbol{\Pi} \, , \tag{A24b}$$

$$\mathbf{E}^{\mathrm{a}} = \mathbf{E}\,\mathbf{U} \, , \tag{A24c}$$

where $\mathbf{H}$ is the linearization of $\mathcal{H}$ in the vicinity of $\mathbf{x}^{\mathrm{b}}$, $\mathbf{H}^p \doteq \mathbf{H}\mathbf{E}$, the columns of $\mathbf{U}$ are ordered orthonormal eigenvectors of $\widetilde{\boldsymbol{\Pi}}^{\mathrm{a}}$ and $\boldsymbol{\Pi}^{\mathrm{a}}$ is diagonal. With the successive corrections, (A24a–c) are repetitively used for each scale w. The Kalman update and (A24a) differ because of the different gains, $\mathbf{K} \doteq \mathbf{P}^{\mathrm{b}}\mathbf{H}^T\left[\mathbf{H}\mathbf{P}^{\mathrm{b}}\mathbf{H}^T + \mathbf{R}\right]^{-1}$ and $\mathbf{K}^p \doteq \mathbf{B}^p\mathbf{H}^T\left[\mathbf{H}\mathbf{B}^p\mathbf{H}^T + \mathbf{R}\right]^{-1}$, respectively. Three cases are discussed in LLA98 as a function of the measurement properties $\mathbf{H}$ and $\mathbf{R}$.

APPENDIX B

Relevant scalings and non-dimensional numbers

Table B defines numbers that are relevant for the present mesoscale to subbasin-scale study. The notation is standard (Gill, 1982; Pedlosky, 1987; Cushman-Roisin, 1994): g is the

acceleration due to gravity; L and D the horizontal and vertical length-scales of motion; U and W the horizontal and vertical characteristic velocity scales; f_0 and β_0 the Coriolis parameter and its northward gradient at latitude θ_0; $\rho_s(z)$ the background density profile; and, ρ_0 a constant reference density. In addition, $N_s = \sqrt{-\frac{g}{\rho_0}\frac{\delta\rho_s}{\delta z}}$ is the Brunt-Väisälä frequency, $R_D = N_s D/f_0$ and $R_{\rm ext} = \sqrt{gD}/f_0$ the internal and external Rossby radius of deformations, and $\nabla_h H$ the horizontal gradient of bottom topography H. Except for g, all of these characteristic scales are regional; they vary with the location and process considered.

Table B. Main non-dimensional numbers/parameters

Number/Parameter	Definition	Ratio
Rossby:	$Ro = \frac{U}{f_0 L}$	Relative vorticity to planetary vorticity (also nonlinear advection to Coriolis force)
External Burger:	$Bu_{\rm ext} = \frac{gD}{f_0^2 L^2} = \frac{R_{\rm ext}^2}{L^2}$	Relative vorticity to external vertical vortex-tube stretching (of free-surface)
Internal Burger:	$Bu = \frac{N_s^2 D^2}{f_0^2 L^2} = \frac{R_D^2}{L^2}$	Relative vorticity to internal vertical vortex-tube stretching (of isopycnal surfaces)
Planetary-β:	$\beta = \beta_0 \cdot \frac{L^2}{U}$	Planetary (ambient) vorticity gradient to relative vorticity gradient
Topographic-β:	$\alpha = \lvert\nabla_h H\rvert \frac{f_0}{D} \cdot \frac{L^2}{U}$	Topographic (ambient) vorticity gradient to relative vorticity gradient
Slope or topographic:	$s = \lvert\nabla_h H\rvert \cdot \frac{L}{D} = \alpha\, Ro$	Topographic gradient to motion aspect ratio

For the synoptic and horizontally isotropic quasi-geostrophic scales in a stratified ocean, Ro, $Bu_{\rm ext}^{-1}$ and $s \ll 1$, but the other numbers may take a range of values: in particular, Bu and α increase with the strength of the stratification and topographic slope, respectively (e.g. Pedlosky, 1987). At these scales, using the internal energy (density) equation to estimate W, one can also show that $\frac{Ro}{Bu}$ is the ratio of vertical convergence to horizontal divergence $\frac{WL}{UD}$, and that the characteristic horizontal variations in density $\Delta\rho$ and vertical variations in background density $\Delta\rho_s$ are related via, $\frac{\Delta\rho}{\rho_0} = \frac{Ro}{Bu}\frac{\Delta\rho_s}{\rho_0}$.

REFERENCES

Abbott, M.R. and R.M. Letelier, 1998. Decorrelation scales of chlorophyll as observed from bio-optical drifters in the California Current. In *Deep-Sea Research II,* **45**, 1639-1667.

Andersson, E., J. Haseler, P. Under, P. Courtier, G. Kelly, D. Vasiljevic, C. Brankovic, C. Cardinali, C. Gaffard, A. Hollingsworth, C. Jakob, P. Janssen, E. Klinker, A. Lanzinger, M. Miller, F. Rabier, A. Simmons, B. Strauss, J-N. Thépaut and P. Viterbo. 1998, The ECMWF implementation of three-dimensional variational assimilation (3D-Var). III: Experimental results. *Q.J.R. Meteorol. Soc.,* **124**, 1831–1860.

Barkmeijer, J., M. Van Gijzen and F. Bouttier, 1998. Singular vectors and estimates of the analysis-error covariance metric. *Q.J.R. Meteorol. Soc.,* **124**, 1695–1713.

Bennett, A.F. and B.S. Chua, 1994. Open-ocean modeling as an inverse problem: the primitive equations. *Mon. Weather Rev.,* **122**(6), 1326–1336.

Brenner, S. 1993. Long-term evolution and dynamics of a persistent warm core eddy in the Eastern Mediterranean Sea. In *Deep-Sea Research II,* **40**(6), 1193–1206.

Brink, K.H. 1991. Coastal-trapped waves and wind-driven currents over the continental shelf *Annu. Rev. Fluid Mech.,* **23**, 389–412.

Carter, E.F. and A.R. Robinson, 1987. Analysis models for the estimation of oceanic fields. *J. Atmos. Oceanic Techno.,* **4**, No. 1, 49–74.

Chin T.M., Mariano, A.J. and E.P. Chassignet, 1999. Spatial regression and multiscale approximations for sequential data assimilation in ocean models. *J. Geophys. Res.-Oceans* **104**, 7991–8014.

Cressie N. and H.C. Huang, 1999. Classes of nonseparable, spatio-temporal stationary covariance functions. *J. Am. Stat. Assoc.* **94**, 1330–1340.

Cushman-Roisin, B., 1994. *Introduction to Physical Oceanography.* Prentice-Hall, Inc.

Daley, R., 1991. *Atmospheric Data Analysis*, Cambridge University Press.

Dee D.P. and A.M. da Silva, 1999. Maximum-likelihood estimation of forecast and observation error covariance parameters. Part I: Methodology. *Mon. Weather Rev.* **127**, 1822–1834.

De Mey, P. and A.R. Robinson, 1987. Assimilation of altimeter eddy fields in a limited area quasi-geostrophic model. *J. Phys. Oceanography,* **17**, (12), 2280–2293.

De Mey, P., 1997. Data assimilation at the oceanic mesoscale: A review. *J. of the Meteorol. Soc. of Japan,* **75**, (1B), 415–427.

Derber J. and F. Bouttier, 1999. A reformulation of the background error covariance in the ECMWF global data assimilation system. *Tellus Ser. A-Dyn. Meteorol. Oceanol.,* **51**, (2), 195–221.

Dewar, W.K. and P.D. Killworth. 1995. On the stability of oceanic rings. *J. Phys. Oceanogr.,* **25**, 1467-1487.

Ehrendorfer, M. 1997. Predicting the uncertainty of numerical weather forecasts: a review. *Meteorologische Zeitschrift,* **6** (4) 147–183.

Everson R., Cornillon P., Sirovich L. and Webber A., 1997. An empirical eigenfunction analysis of sea surface temperatures in the western North Atlantic. *J. Phys. Oceanogr.,* **27**, (3), 468–479.

Franke, R. and E. Barker, 2000. Vertical correlation functions for temperature and relative humidity errors. *Mon. Weather Rev* **128**, (12), 3962–3981.

Fukumori, I. and P. Malanotte-Rizzoli, 1995. An approximate Kalman filter for ocean data assimilation: An example with one idealized Gulf Stream Model, *J. Geophys. Res.,* **100**, 6777–6793.

Gaspari, G. and S.E. Cohn, 1999. Construction of correlation functions in two and three dimensions.

Q. J. R. Meteorol. Soc. **125**, 723–757.

Gill, A.E., 1982. *Atmosphere-Ocean Dynamics.* Academic Press. International Geophysics Series, **30**.

GISIS, 1995. User Guide for GISIS version 1.0, German Remote sensing data center (DFD), DLR, Issue 0.7, S. White (Ed.), 38pp.

Gneiting T., 1999. Correlation functions for atmospheric data analysis. *Q. J. R. Meteorol. Soc.* **125**, 2449–2464.

Hamill T.M., Whitaker J.S. and C. Snyder. 2001. Distance-dependent filtering of background error covariance estimates in an ensemble Kalman filter. *Mon. Weather Rev.* **129** (11): 2776–2790.

Haney R.L., R.A. Hale, C.A. Collins, 1995. Estimating subpycnocline density-fluctuations in the California current region from upper ocean observations. *J. Atmos. Oceanic Technol.,* **12**, (3), 550–566.

Hecht, A., N. Pinardi, and A.R. Robinson, 1988. Currents, water masses, eddies and jets in the Mediterranean Levantine Basin. *J. Phys. Oceanography,* **18**(10), 1320–1353.

Holland D.M. and I.T. Webster, 1994. The effects of stratification and alongshore currents on the propagation of coastal-trapped waves. *Continental Shelf Research,* **14**, 57–77.

Huthnance, J.M., 1978. On coastal trapped waves: analysis and numerical calculation by inverse iteration. *J. Phys. Oceanogr.,* **8**, 74–92.

Huthnance, J.M., 1992. Extensive slope currents and the ocean-shelf boundary. *Prog. Oceanog.,* **29**, 161–192.

Ide, K., P. Courtier, M. Ghil, and A. C. Lorenc, 1997. Unified notation for data assimilation: operational, sequential and variational. *J. of the Meteorol. Soc. of Japan,* **75**, (1B), 181-189.

Kaplan, A., Y. Kushnir, M.A. Cane and M.B. Blumenthal, 1997. Reduced space optimal analysis for historical data sets: 136 years of Atlantic sea surface temperatures. *J. Geophys. Res.,* **102** (C13), 27835–27860.

Keppenne, C. L., 2000. Data assimilation into a primitive equation model using a parallel ensemble Kalman filter, Mon. Wea. Rev., 128, 1971-1981.

Killworth, P.D., J.R. Blundell and W.K. Dewar. 1997. Primitive equation instability of wide oceanic rings. Part I: linear theory. 27 941-962.

LeBlond, P.H. and Mysak, L.A., 1971. Waves in the ocean, Elsevier, Amsterdam, 602pp.

Lermusiaux, P.F.J. 1997. Error subspace data assimilation methods for ocean field estimation: theory, validation and applications. PhD Thesis, May 1997, Harvard Univ., Cambridge, MA.

Lermusiaux P.F.J., C.J. Lozano and D.G.M. Anderson, 1998. On the mapping of multivariate geophysical fields: studies of the sensitivity to error subspace parameters. Harvard Report in Physical/Interdisciplinary Ocean Science. No. 58.

Lermusiaux, P.F.J. and A.R. Robinson, 1999. Data assimilation via error subspace statistical estimation, Part I: theory and schemes. *Mon. Weather Rev.* **127**(7), 1385–1407.

Lermusiaux, P.F.J. 1999a. Data assimilation via error subspace statistical estimation, Part II: Middle Atlantic Bight shelfbreak front simulations and ESSE validation. *Mon. Weather Rev.* **127**(7), 1408–1432.

Lermusiaux, P.F.J. 1999b. Estimation and study of mesoscale variability in the Strait of Sicily. *Dyn. of Atmos. Oceans*, Special issue in honor of Professor A.R. Robinson, **29**, 255–303.

Lermusiaux, P.F.J., D.G.M. Anderson and C.J. Lozano, 2000. On the mapping of multivariate geophysical fields: error and variability subspace estimates. *Q.J.R. Meteorol. Soc.*, April B, 1387–1430.

Lermusiaux, P.F.J. 2001. Evolving the subspace of the three-dimensional multiscale ocean variability: Massachusetts Bay. *J. Marine Systems*, Special issue on "Three-dimensional ocean circulation: Lagrangian measurements and diagnostic analyses", **29**, 385–422.

Lermusiaux, P.F.J. and A.R. Robinson, 2001. Features of dominant mesoscale variability, circulation patterns and dynamics in the Strait of Sicily. *Deep Sea Research, Part I.* **48**, (9), 1953-1997.

Lorenc, A.C., 1992. Iterative analysis using covariance functions and filters. *Q.J.R. Meteorol. Soc.,* **118**, 569–591.

Louis, A.K., Maass, P. and Rieder, A., 1997. *Wavelets theory and applications.* Pure and applied mathematics, A Wiley-interscience series of texts, monographs and tracts. J. Wiley and Sons.

Lozano, C.J., A.R. Robinson, H.G. Arango, A. Gangopadhyay, N.Q. Sloan, P.J. Haley, and W.G. Leslie, 1996. An interdisciplinary ocean prediction system: Assimilation strategies and structured data models. *Modern Approaches to Data Assimilation in Ocean Modelling*, P. Malanotte-Rizzoli, ed., Elsevier Oceanography Series, Elsevier Science, The Netherlands.

Malanotte-Rizzoli, P., A.R. Robinson, W. Roether, B. Manca, A. Bergamasco, S. Brenner, G. civitarese, D. Georgopoulos, P.J. Haley, S. Kioroglou, H. Kontoyannis, N. Kress, M.A. Latif, W.G. Leslie, E. Ozsoy, M. Ribera d'Alcala, I. Salihoglu, E. Sansone, and A. Theocharis, 1996. Experiment in Eastern Mediterranean probes origin of deep water masses. *EOS,* **77**(32).

Malanotte-Rizzoli, P., Manca, B.B., d'Alcala, M.R., Theocharis, A., Brenner, S., Budillon, G. and E. Ozsoy, 1999. The Eastern Mediterranean in the 80s and in the 90s: the big transition in the intermediate and deep circulations. *Dyn. of Atmos. Oceans*, Special issue in honor of Prof. A.R. Robinson, **29**, 365–395.

Menemenlis D. and M. Chechelnitsky, 2000. Error estimates for an ocean general circulation model from altimeter and acoustic tomography data. *Mon. Weather Rev.* **128**, (3), 763–778.

Miller, A.J. and B.D. Cornuelle, 1999. Forecasts from fits of frontal fluctuations. *Dyn. of Atmos. Oceans*, Special issue in honor of Professor A.R. Robinson, **29**, 305–333.

Milliff, R.F. and A.R. Robinson, 1992. Structure and dynamics of the Rhodes Gyre System and dynamical interpolation for estimates of the mesoscale variability. *J. Phys. Oceanography,* **22**(4), 317–337.

Mitchell H.L. and P.L Houtekamer, 2000. An adaptive ensemble Kalman filter. *Mon. Weather Rev.* **18**, (2), 416–433.

Molinari R.L. and J.F. Festa, 2000. Effect of subjective choices on the objective analysis of sea surface temperature data in the tropical Atlantic and Pacific oceans. *Oceanol. Acta* **23**, (1), 3–14.

Molteni, F., R. Buizza, T.N. Palmer and T. Petroliagis, 1996. The ECMWF ensemble prediction system. Methodology and validation. *Q.J.R. Meteorol. Soc.,* **122**, 73–119.

Nittis K. and A. Lascaratos, 1998. Diagnostic and prognostic numerical studies of LIW formation. *J. Marine Syst.* **18**, (1-3), 179–195.

Pedder M. and D. Gomis, 1998. Applications of EOF analysis to the spatial estimation of circulation features in the ocean sampled by high-resolution CTD soundings. *J. Atmos. Oceanic Techno.,* **15**, (4), 959–978.

Pedlosky, J. 1987. *Geophysical Fluid Dynamics.* Second edition, Springer-Verlag.

Orlanski, I. 1976. A simple boundary condition for unbounded hyperbolic flows. *J. Comput. Phys.,* **41**, 251–269.

Özsoy, E., H. Hecht, Ü. Ünlüata, S. Brenner, H.I. Sur, J. Bishop, M.A. Latif, A. Rozentraub, and T. Oğuz, 1993. A synthesis of the Levantine Basin circulation and hydrography, 1985–1990. In *Deep-Sea Res. II,* **40**(6), 1175–1119.

Rabier, F., A. McNally, E. Andersson, P. Courtier, P. Unden, J. Eyre, A. Hollingsworth, and F. Bouttier, 1998. The ECMWF implementation of three-dimensional variational assimilation (3D-Var). II: Structure functions. *Q.J.R. Meteorol. Soc.,* **124**, 1809-1829.

Reichle R.H., McLaughlin D.B. and D. Entekhabi, 2002. Hydrologic data assimilation with the ensemble Kalman filter. *Mon. Weather Rev.,* **130**, (1): 103–114.

Riishojgaard, L.P. 1998. A direct way of specifying flow-dependent background error correlations for meteorological analysis systems. *Tellus Ser. A-Dyn. Meteorol. Oceanol.,* **50**, 42–57.

Robinson, A.R. and M. Golnaraghi, 1993. Circulation and dynamics of the Eastern Mediterranean Sea; quasi-synoptic data-driven simulations. In *Deep-Sea Res. II.* **40**(6), 1207–1246.

Robinson A.R. and P. Malanotte-Rizzoli (guest Eds.), 1993. Topical studies in oceanography. In *Deep-Sea Res., II,* **40**(6), Milliman, J.D. (Ed.), 1073–1329.

Robinson, A.R., 1996. Physical processes, field estimation and an approach to interdisciplinary ocean modeling. *Earth-Science Rev.,* **40**, 3–54.

Robinson, A.R., P.F.J. Lermusiaux and N.Q. Sloan, III, 1998. Data Assimilation, in *The Sea: The Global Coastal Ocean I*, Processes and Methods (K.H. Brink and A.R. Robinson, editors), Volume 10, John Wiley and Sons, New York, NY.

Robinson, A.R., 1999. Forecasting and simulating coastal ocean processes and variabilities with the Harvard Ocean Prediction System, in *Coastal Ocean Prediction*, (C.N.K. Mooers, Ed.), AGU Coastal and Estuarine Studies Series, 77–100.

Robinson A.R. and P.F.J. Lermusiaux, 2001. Data assimilation for modeling and predicting coupled physical-biological interactions in the sea. In "*The Sea: Volume 12: Biological-Physical Interactions in the Ocean.*", Robinson, A.R., J.R. McCarthy and B.J. Rothschild (Eds.). In press.

Roether, W., B.B. Manca, B. Klein, D. Bregant, D. Georgopoulos, V. Beitzel, V. Kovačević, and A. Luchetta, 1996. Recent changes in Eastern Mediterranean deep waters. *Science,* **271**, 333–335.

Shapiro, R., 1970. Smoothing, filtering, and boundary effects. *Rev. Geophys. and Space Phys.,* **8**(2), 359–387.

Smith, P.C., 1983. Eddies and coastal interactions. In *Eddies in marine science*, A.R. Robinson (Ed), 446–480.

Tippett M.K., Cohn, S.E., Todling, R. and D. Marchesin, 2000. Low-dimensional representation of error covariance. *Tellus Ser. A-Dyn. Meteorol. Oceanol.* **52**, (5), 533–553.

Thacker, W.C. and Lewandowicz, R., 1996. Climatic indices, principal components, and the Gauss-Markov theorem. *J. Climate,* **9**, (8), 1942–58.

Thacker, W.C. and Lewandowicz, R., 1997. A comparison of low-dimensional representations of sea-surface temperature anomalies in the North Atlantic. *Int. J. of Clim.,* **17**, (9), 953–67.

Toth Z. and Kalnay E., 1997. Ensemble forecasting at NCEP and the breeding method. *Mon. Weather Rev.* **125**, (12), 3297–3319.

Verron, J., Gourdeau, L., Pham, D.T., Murtugudde, R. and Busalacchi, A.J, 1999. An extended Kalman filter to assimilate satellite altimeter data into a nonlinear numerical model of the tropical Pacific Ocean: Method and validation. *J. Geophys. Res.-Oceans* **104**, 5441–5458.

von Storch, Hans and Claude Frankignoul, 1998. Empirical modal decomposition in coastal oceanography. In *The Sea: The Global Coastal Ocean I*, Processes and Methods (K.H. Brink and A.R. Robinson, Eds.), Volume 10, John Wiley and Sons, New York, NY.

Wunsch, C., 1997. The vertical partition of oceanic horizontal kinetic energy. *J. Phys. Oceanogr.,* **27**, (8), 1770–94.

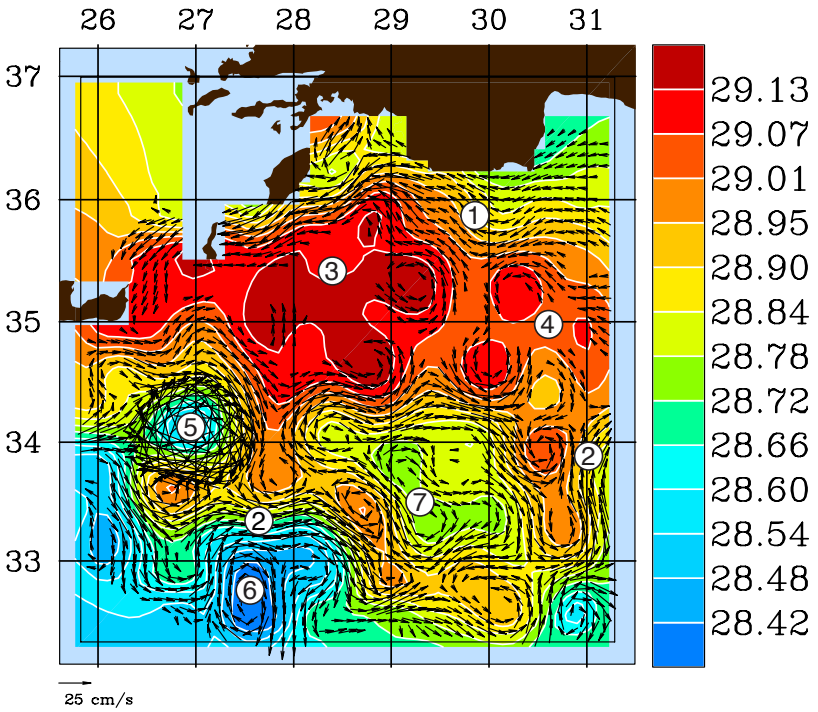

Fig. 1. March 27 analysis (nowcast) for Case 4 (see Sect. 4) of the potential density σ_θ at 105 m, overlaid with the horizontal velocity vectors at 5 m (vectors are plotted only if the analyzed $||\mathbf{u}||$ is larger than 6 cm/s). The numbers identify the location of the main upper-thermocline features: Asia Minor Current (1), Mid-Mediterranean Jet (2), Rhodes Gyre (3), West Cyprus Gyre (4), Ierapetra Eddy (5), a lobe of the Mersa Matruh Gyre (6) and main anticyclone in the Mersa Matruh-Shikmona Gyre complex (7). Several water masses of the Levantine are clearly visible. For the geography and bathymetry, see Fig. 8a of LAL00; for cartoons of the circulation, see Fig. 2 of Robinson and Golnaraghi (1993).

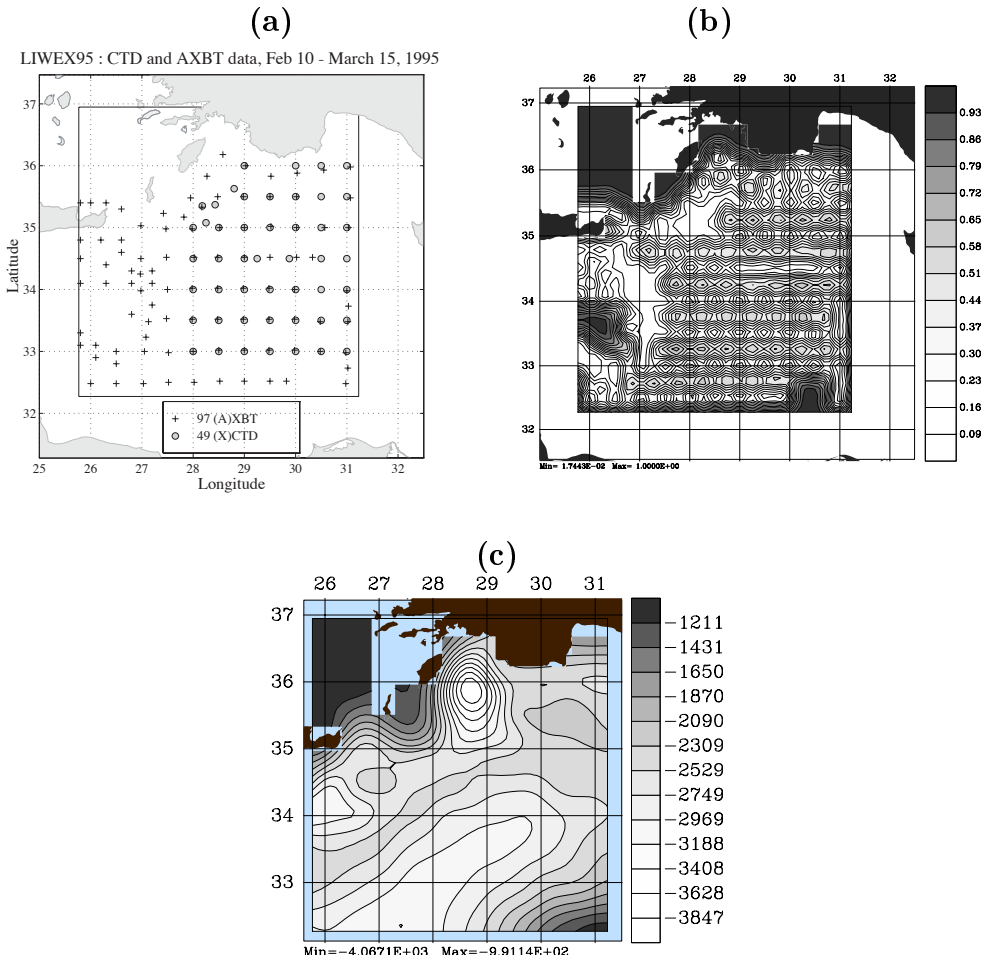

Fig. 2. (a): coordinates of 146 hydrographic profiles that form $\mathbf{y}^o$ (App. A) in the mappings of Sect. 3. They originated from CTD (Conductivity-Temperature-Depth) and AXBT (Aircraft-Deployed Expendable Bathythermographs) observations gathered during February 10–18 and on March 15, 1995, respectively. (b): surface (5 m) *a posteriori* mesoscale error variance for temperature, as estimated by the univariate 2D scheme. Errors are normalized (0–1) and computed using a "Mexican hat" for *a priori* covariance function (60 km zero-crossings, 30 km decay-scales) and an *a priori* error variance of uniform amplitude 1. (c): model bottom topography (m) at tracer grid points.

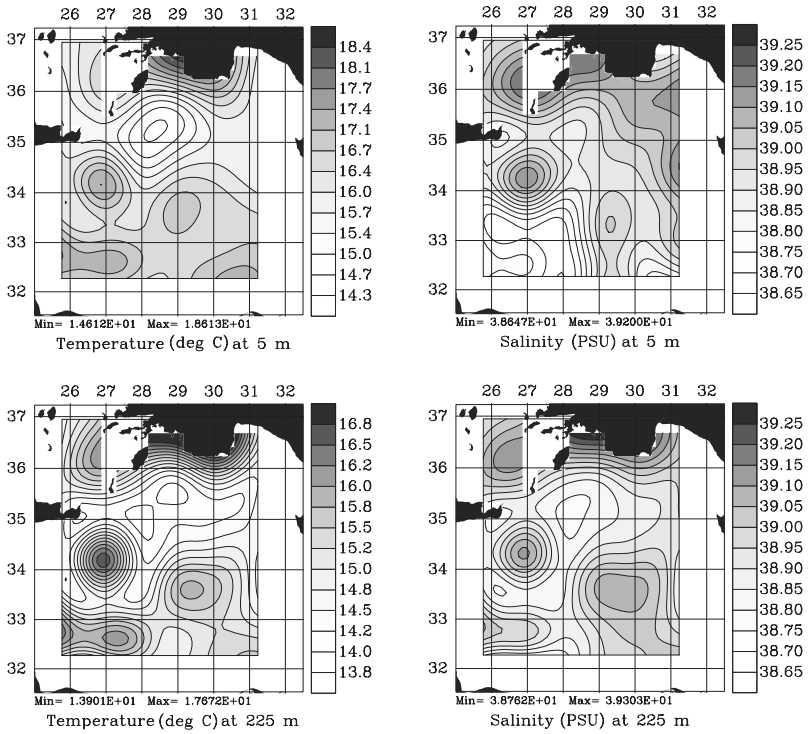

Fig. 3. Subbasin-scale ($w = 1$) temperature and salinity fields, at 5 and 225 m, as estimated by univariate two-dimensional HOPS analyses. The scaling for temperature at 5 m differs from that at 225 m. The scaling for salinity is uniform with depth.

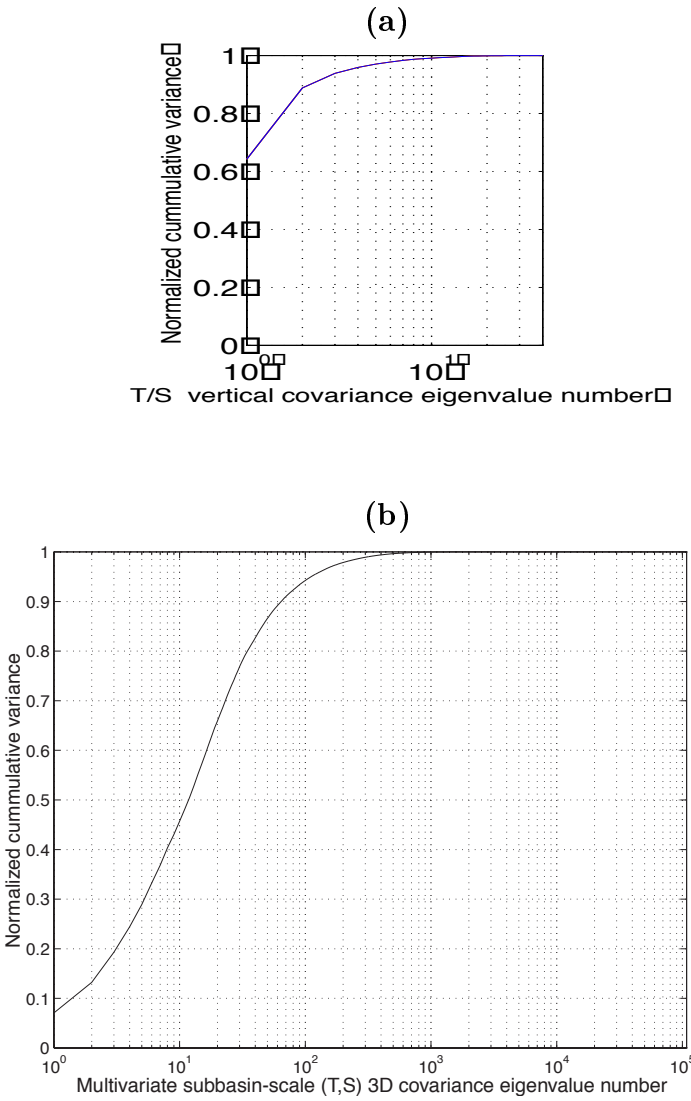

Fig. 4.

(a): Normalized cumulative variance of the subbasin-scale residuals of the tracer profiles, as a function of the eigenvalue number. The covariance $\mathbf{C}^z_{\rm trc}$ is $[40 \times 40]$. The first T, S vertical EOF explains 64% of the subbasin-scale variance, the second 25%, third 5% and fourth 2%. They account together for 96% of the variance; the dominant 8 for 99%.

(b): Normalized cumulative variance of the subbasin-scale error covariance of the 3D tracer fields, $\mathbf{B}_{\rm trc}$ (eq. A13), as a function of the eigenvalue number. The size of $\mathbf{B}_{\rm trc}$ is $[108120 \times 108120]$. The dominant 10 eigenvectors explain 46% of the variance, the dominant 100, 94.25%, dominant 250, 98.5%, and dominant 500, 99.6%. Employing 100 instead of 108120 vectors reduces complexity by more than 10^3 while only missing 6% of the variance.

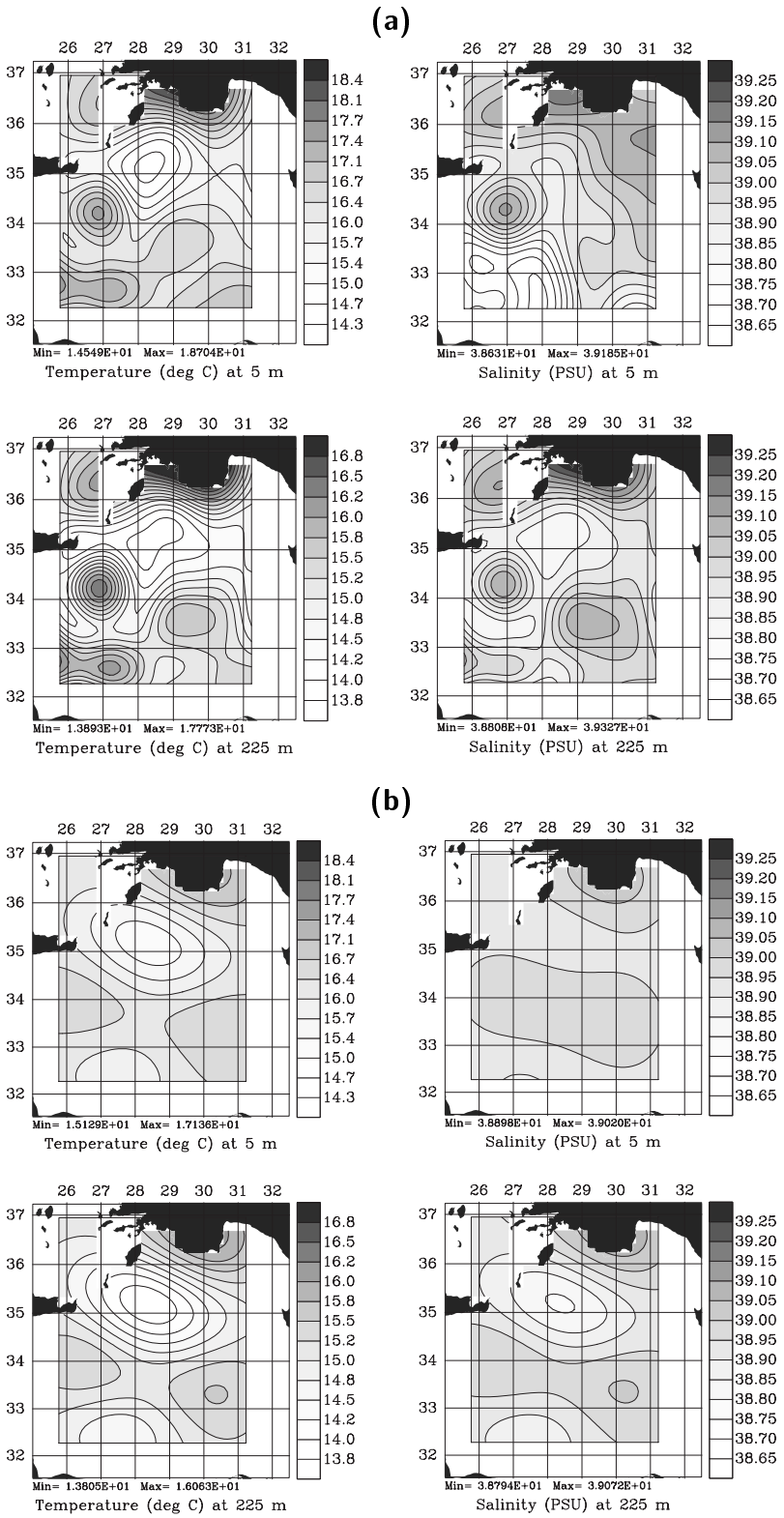

Fig. 5. (a): Subbasin-scale ($w = 1$) temperature and salinity fields, at 5 and 225 m, as estimated by a multivariate 3D error subspace analysis. The dominant 500 vectors of $\mathbf{B}_{\mathrm{trc}}$ are used (eq. A16). Scalings and levels shown are as on Fig. 3. (b): As (a), but with the dominant 10 vectors of $\mathbf{B}_{\mathrm{trc}}$.

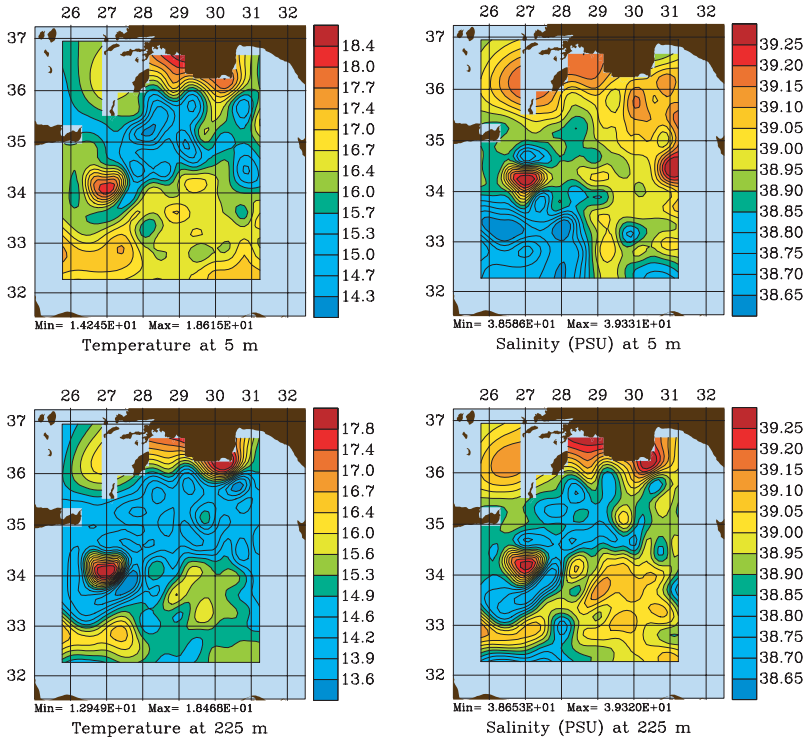

Fig. 6. Total (subbasin-scale plus mesoscale) T and S fields at 5 and 225 m, as estimated by univariate two-dimensional HOPS analyses. The *a priori* estimate $\mathbf{x}^{\mathrm{b}}_{\mathrm{trc}}$ in this second-stage ($w = 2$) is the subbasin-scale analysis of the first-stage ($w = 1$), see Fig. 3. For temperature, the scaling at 5 m differs from that on Fig. 3; for salinity, it is the same.

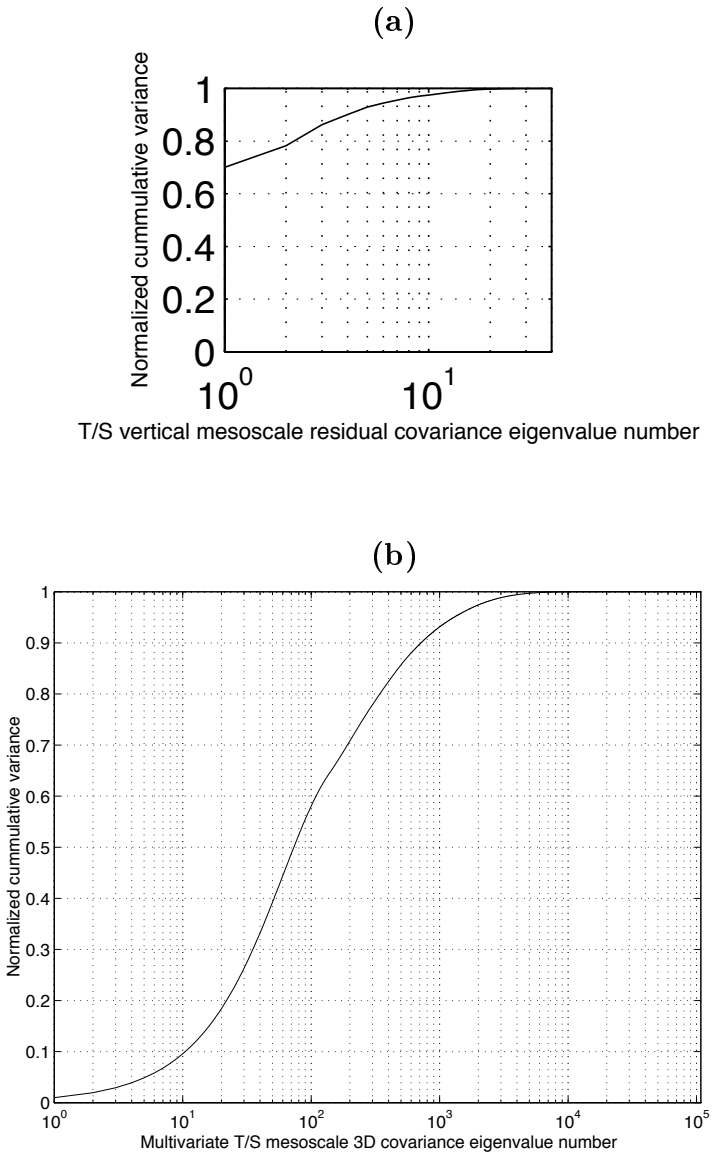

Fig. 7.

(a): As for Fig. 4a, but for the mesoscale residuals of the tracer profiles. The first T, S vertical EOF explains 70% of the mesoscale variance, the second 8%, third 7% and fourth less than 4%.

(b): As for Fig. 4b, but for the mesoscale error covariance of the 3D tracer fields, $\mathbf{B}_{\rm trc}$ (eq. A13). The dominant 100 eigenvectors explain 58% of the variance, the dominant 250, 75%, dominant 500, 86%, and dominant 750, 90.5%.

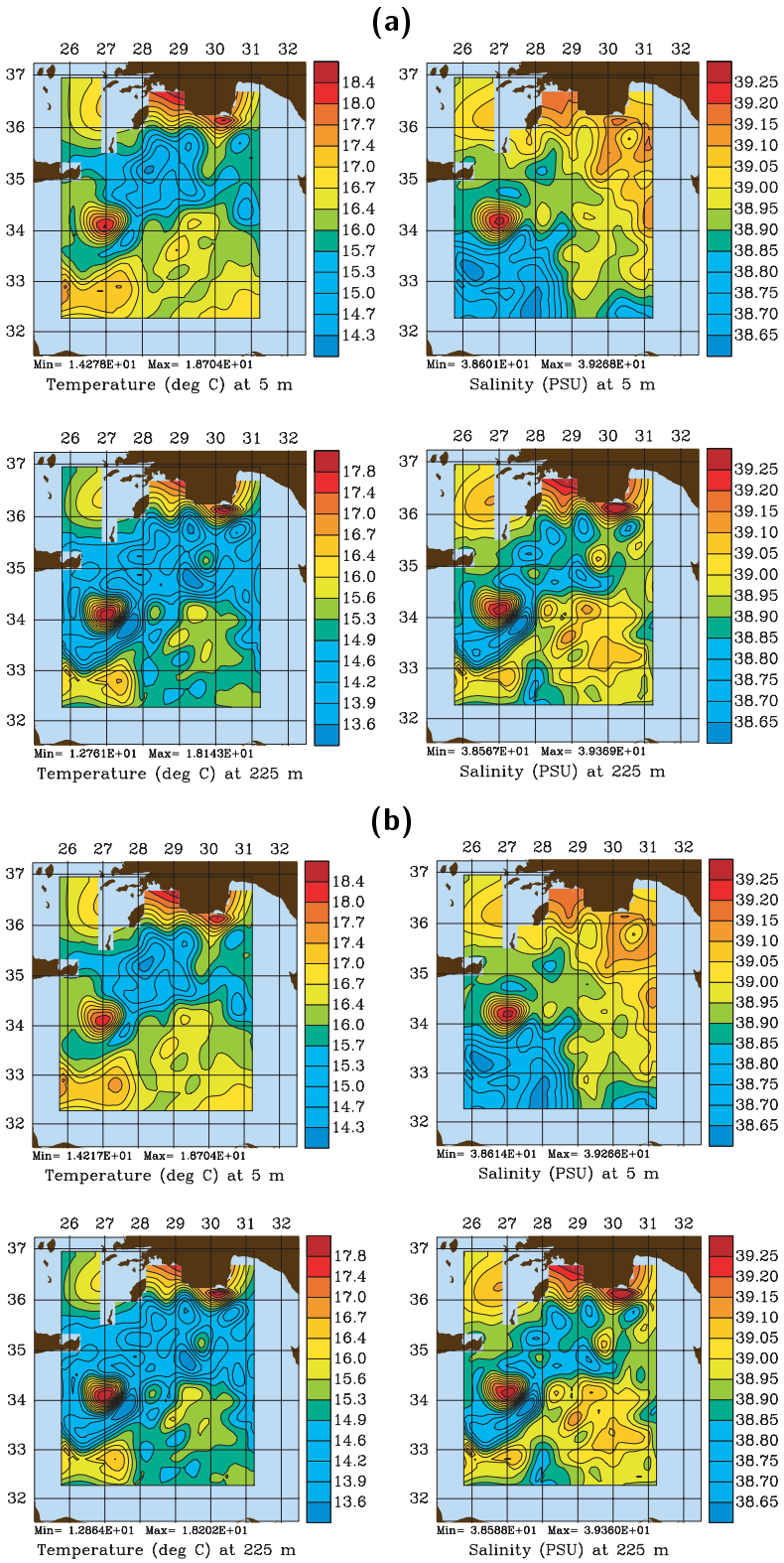

Fig. 8. (a): Total (subbasin-scale plus mesoscale) T and S fields at 5 and 225 m, as estimated by a multivariate 3D error subspace analysis ($w = 2$). The *a priori* estimate $\mathbf{x}^{\mathrm{b}}_{\mathrm{trc}}$ was ilustrated on Fig. 5a. The dominant 500 vectors of $\mathbf{B}_{\mathrm{trc}}$ are used (eq. A16). Scalings are as on Fig. 6. (b): As (a), but with the dominant 750 vectors of $\mathbf{B}_{\mathrm{trc}}$.

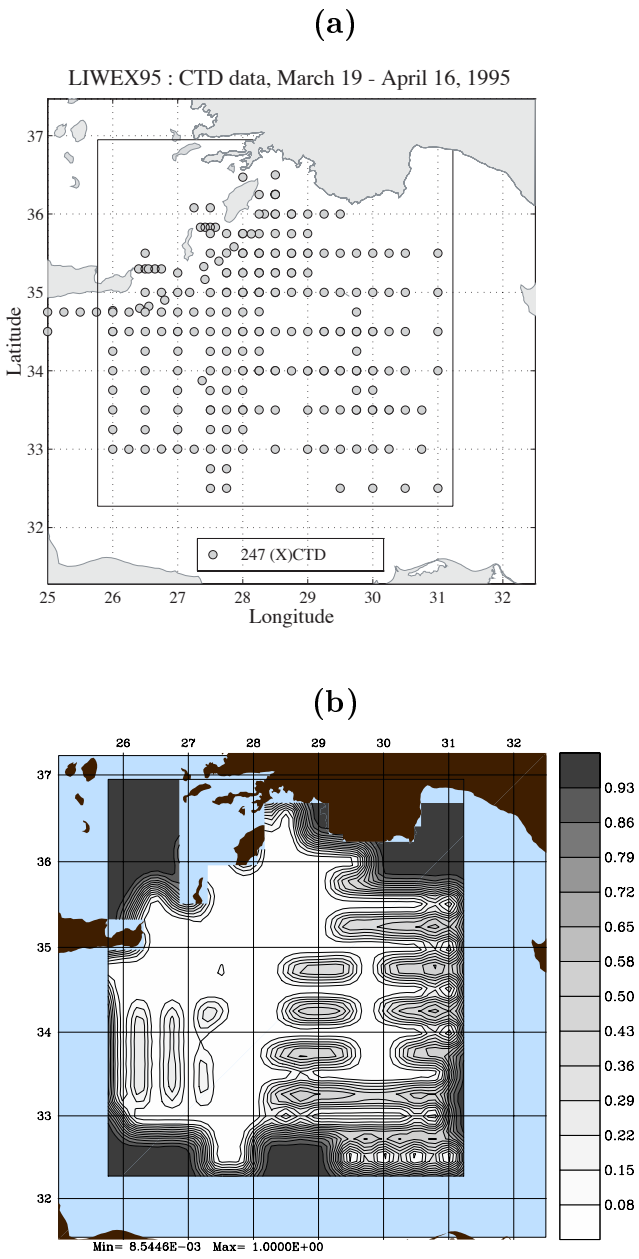

Fig. 9. (a): coordinates of the 247 CTD profiles gathered during March 19–April 16, 236 of which are in the domain and form $\mathbf{y}^o$ (App. A) in the mesoscale mappings. (b): As on Fig. 2b, surface (5 m) normalized *a posteriori* mesoscale error variance, but for the data of Fig. 9a.

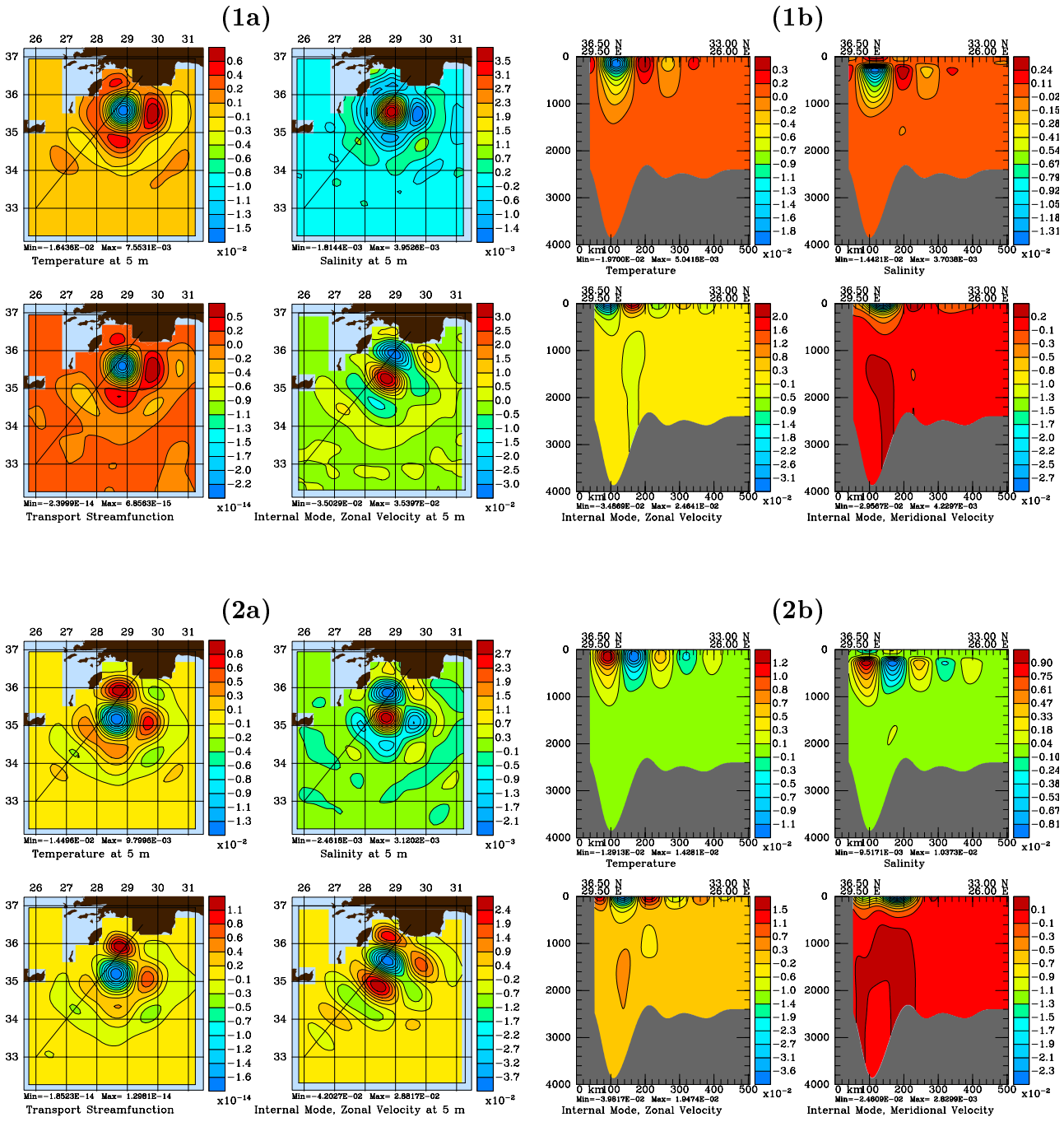

Fig. 10. First two multivariate eigenvectors of the normalized *a priori* mesoscale error covariance, as estimated by Case 2 (Table 1). The Panel number is the vector number, with index (a) for the surface (5 m) level, and (b) for a vertical cross-section parallel to the Cretan Arc, above the Cretan–Rhodes Ridge (section position drawn on Panel a). The estimation is based on App. A.2. All variables are non-dimensional.

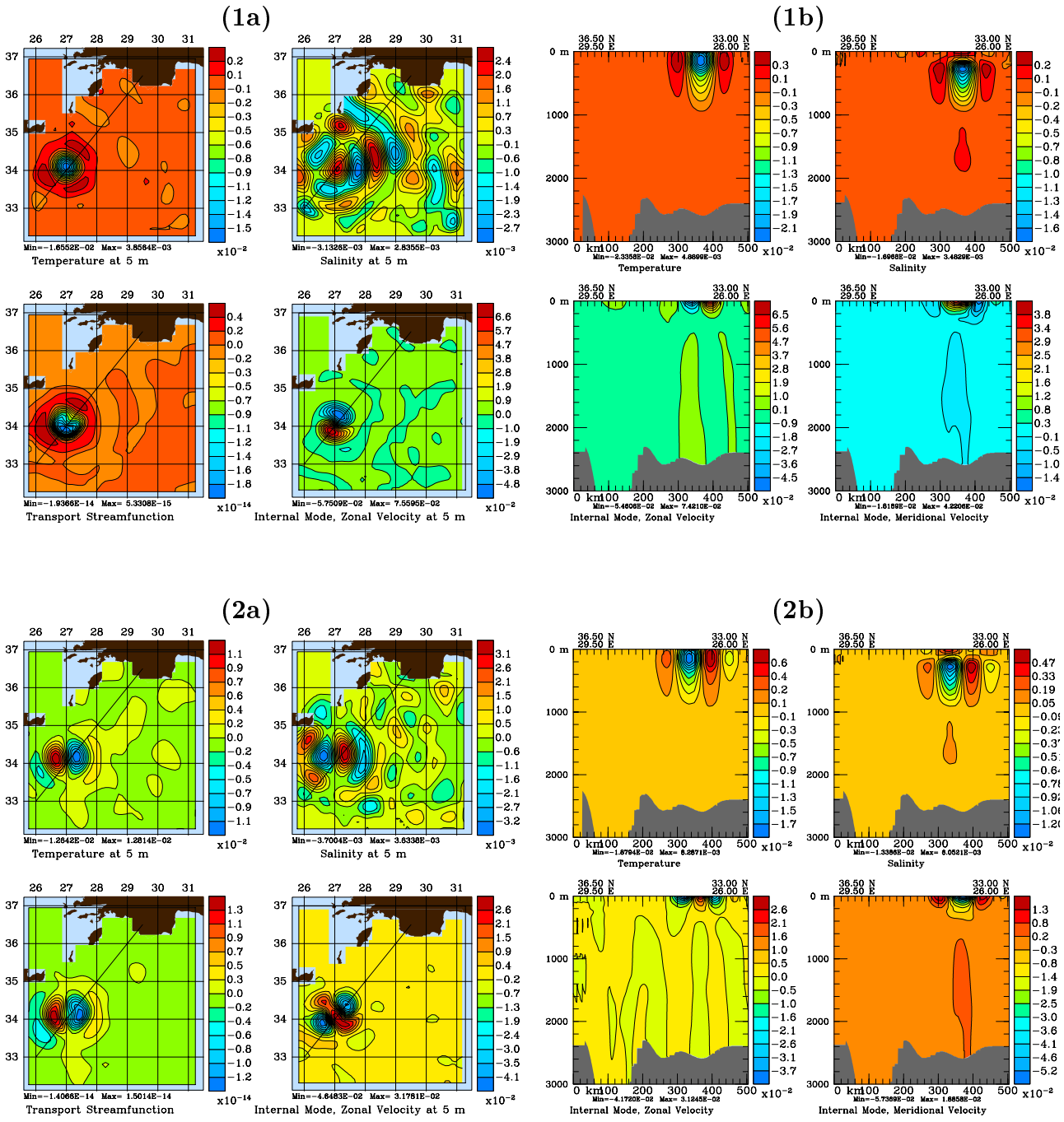

Fig. 11. Same as Fig. 10, but for Case 3 (Table 1) and with a different depth range in the cross-sections.

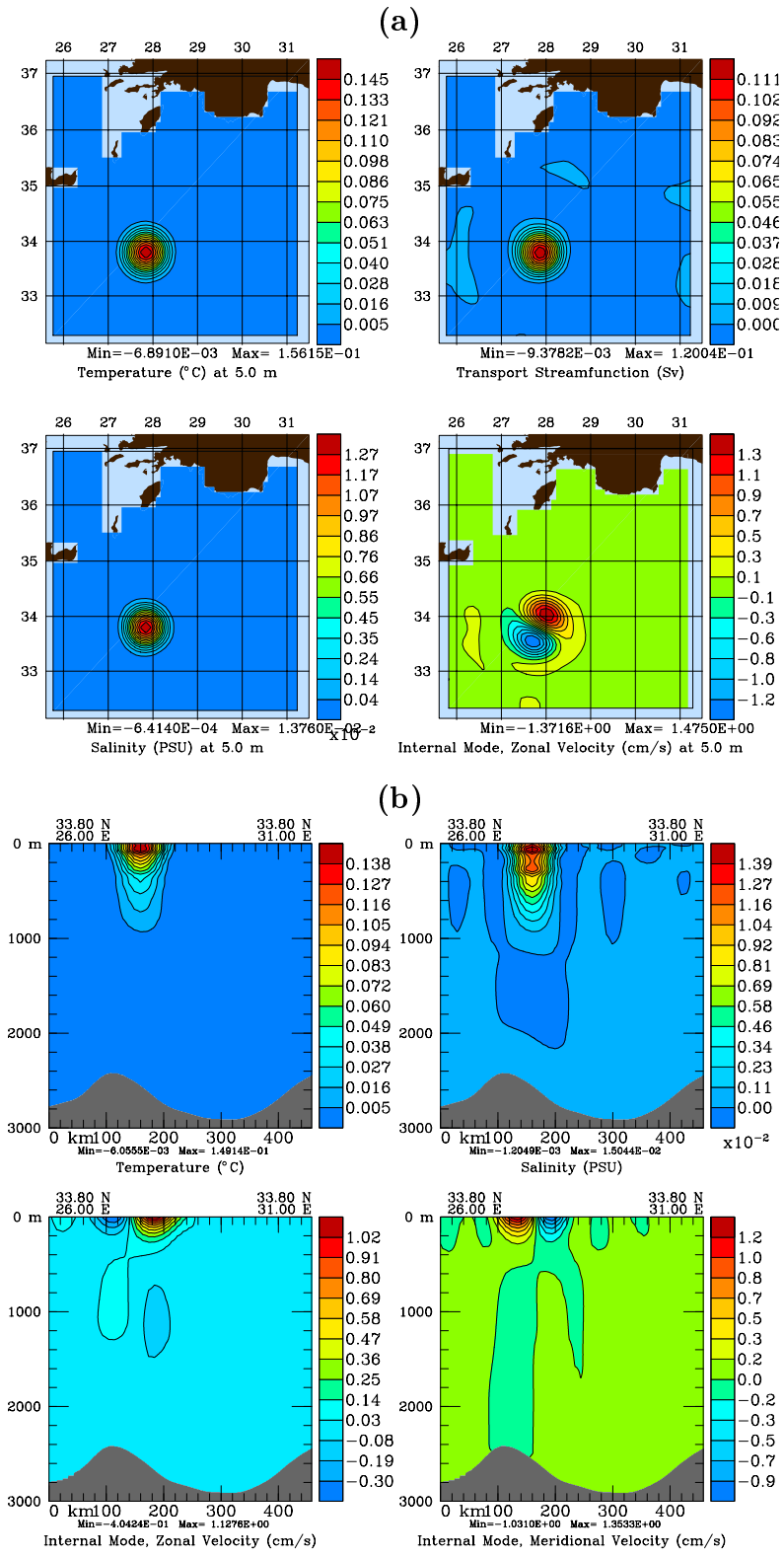

Fig. 12. Case 2 estimate of the dimensional mesoscale covariance functions between the 5 m temperature at (33.80N,27.85E) and the other state variables (only the later are listed in bottom labels, e.g. "T (°C)" stands for "T–T covariance (°C^2)", "S (PSU)" for "T–S covariance (°C PSU)", etc). (a): values on the first level (5 m); (b): zonal cross-sections along 33.80N.

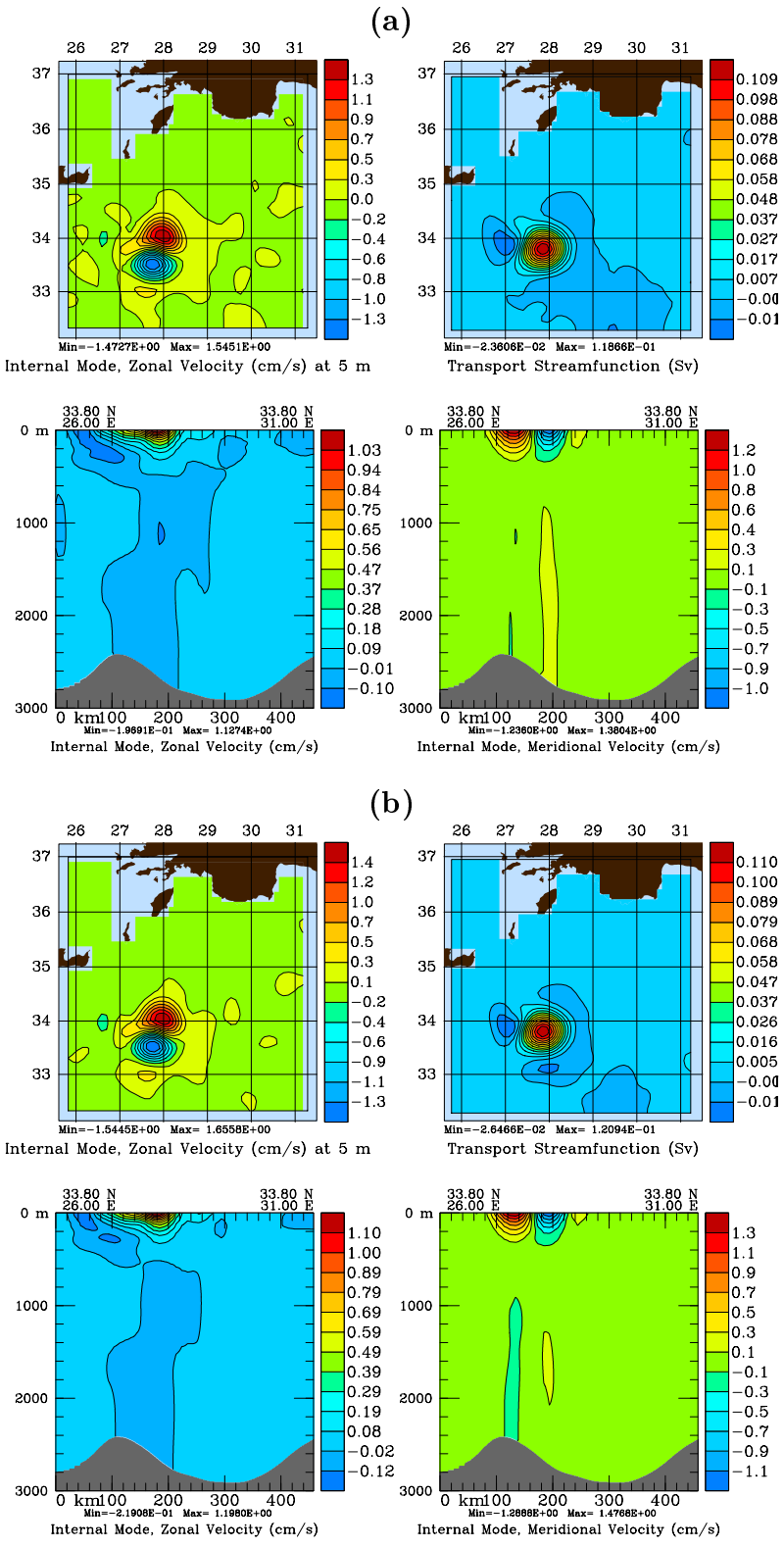

Fig. 13. As Fig. 12, but (a): for Case 3, (b): for Case 4, and only plotting temperature-velocity cross-covariance functions. These functions are still shown on the first level (5 m) and in zonal cross-sections along 33.80N.

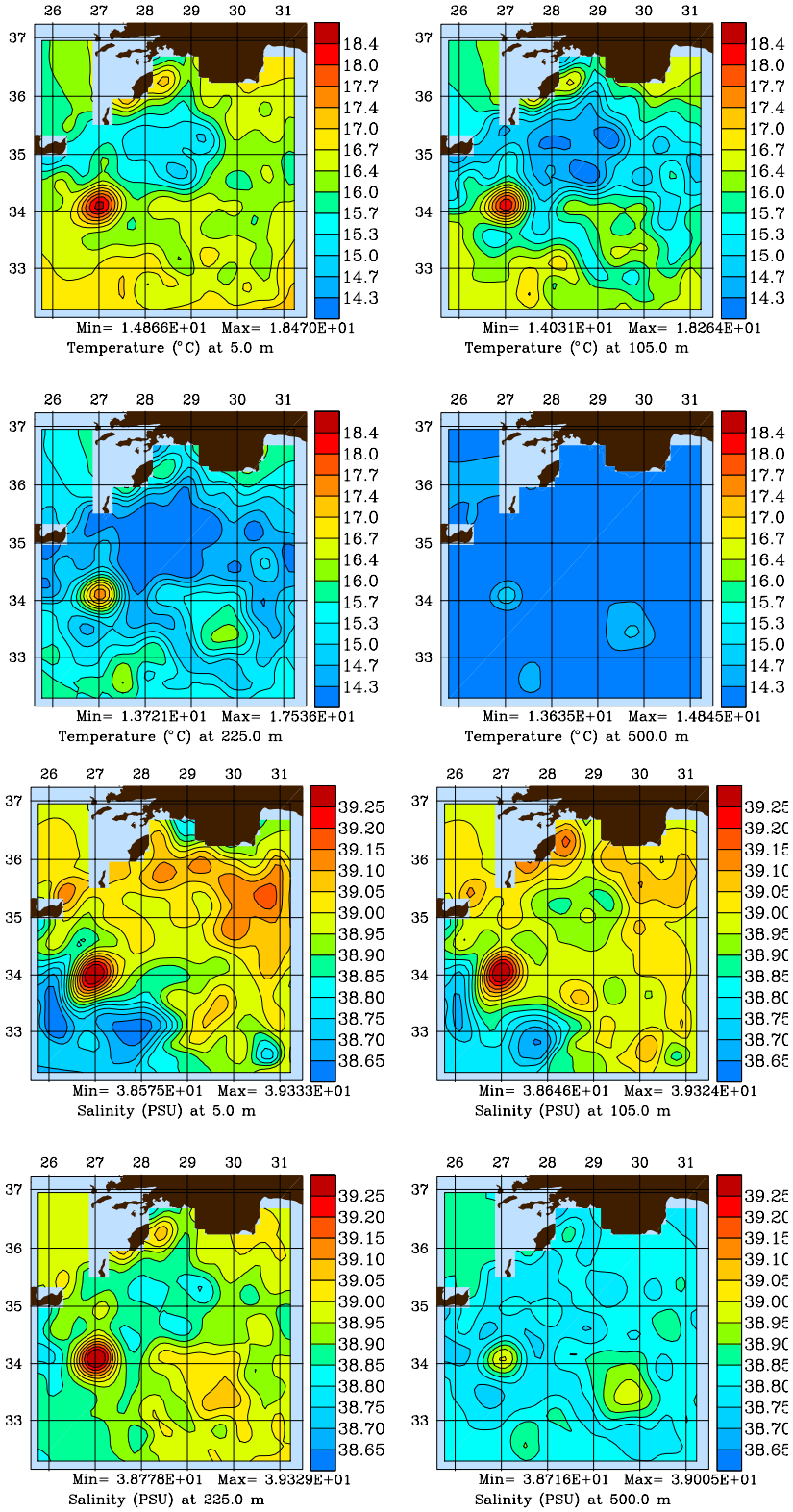

Fig. 14. Case 2: Total (subbasin-scale plus mesoscale) T and S fields resulting from a multivariate 3D analysis. The dominant 322 vectors of $\mathbf{B}^p$ in (eq. A23) are used. The levels shown and scalings are as on Figs. 9–10 of LAL00. The corresponding first-stage fields resulted from a subbasin-scale multivariate 3D analysis.

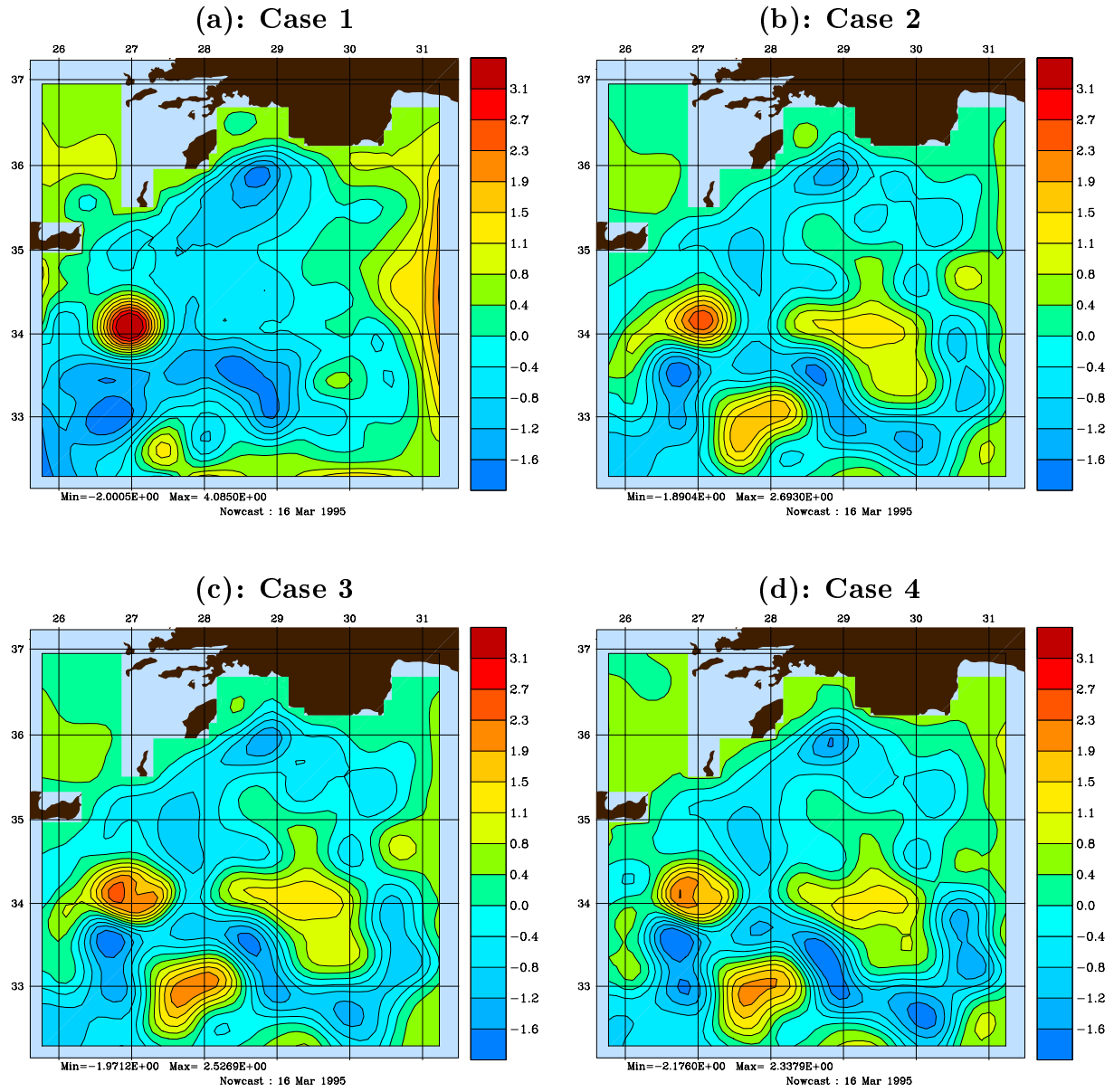

Fig. 15. Total (subbasin-scale plus mesoscale) barotropic transport stream function estimates (ψ in Sv.). (a): univariate 2D scheme. (b): multivariate 3D analysis, with $p = 322$ and linear momentum adjustment. (c): as (b), but with a nonlinear momentum adjustment. (d): as (c), but with $p = 400$ vectors.

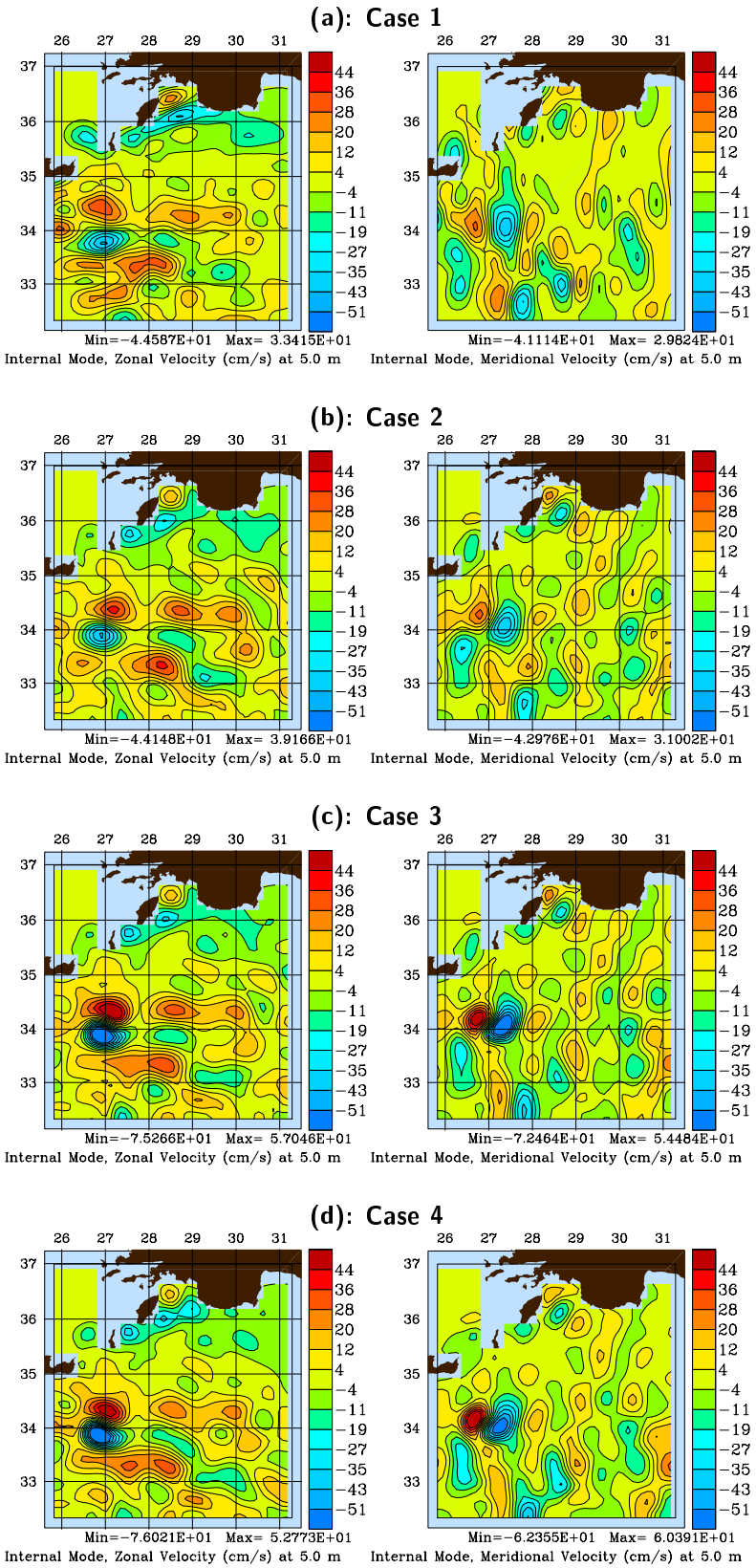

Fig. 16. Total (subbasin-scale plus mesoscale), zero-vertical mean, internal velocity estimates $(\widehat{u}, \widehat{v})$ at 5 m (Cases as on Fig. 15).

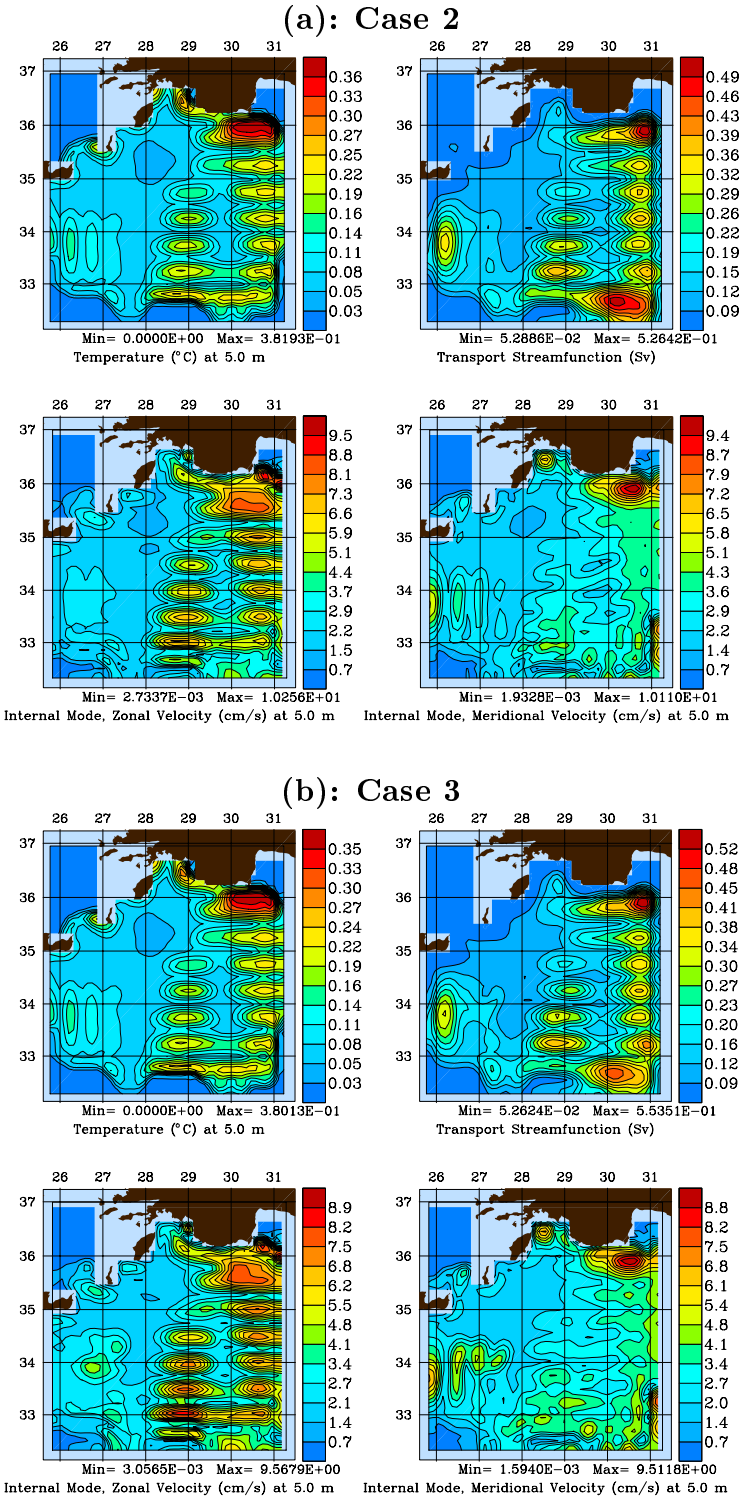

Fig. 17. (a): Multivariate *a posteriori* error standard deviations (St.Dv.) for Case 2. The square root of the diagonal of $\mathbf{E}^{\mathrm{a}}\boldsymbol{\Pi}^{\mathrm{a}}\mathbf{E}^{\mathrm{a}\,T}$ (App. A.3) is illustrated: the surface (5 m) error St.Dv. of T, $\widehat{u}$ and $\widehat{v}$, and the ψ error St.Dv are shown. (b): As (a), but for Case 3.

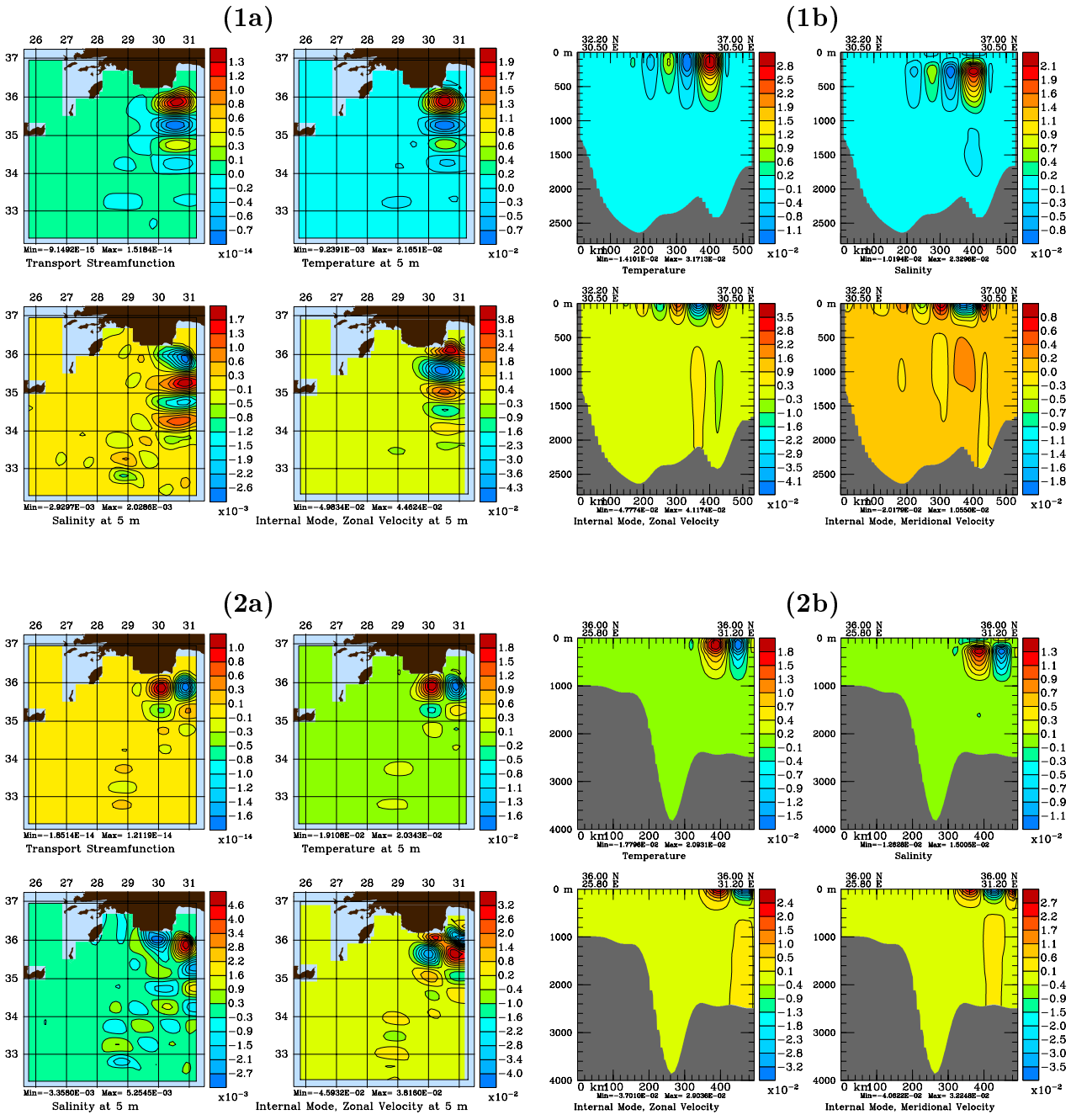

Fig. 18. First two multivariate eigenvectors of the normalized *a posteriori* mesoscale error covariance (columns of $\mathbf{E}^{a^*}$, App. A.3), as estimated by Case 2. The Panel number is the vector number, with index (a) for the surface (5 m) level, and (b) for a vertical cross-section along an axis of large amplitudes (30.50E for vector 1, 36N for vector 2). All variables are non-dimensional.

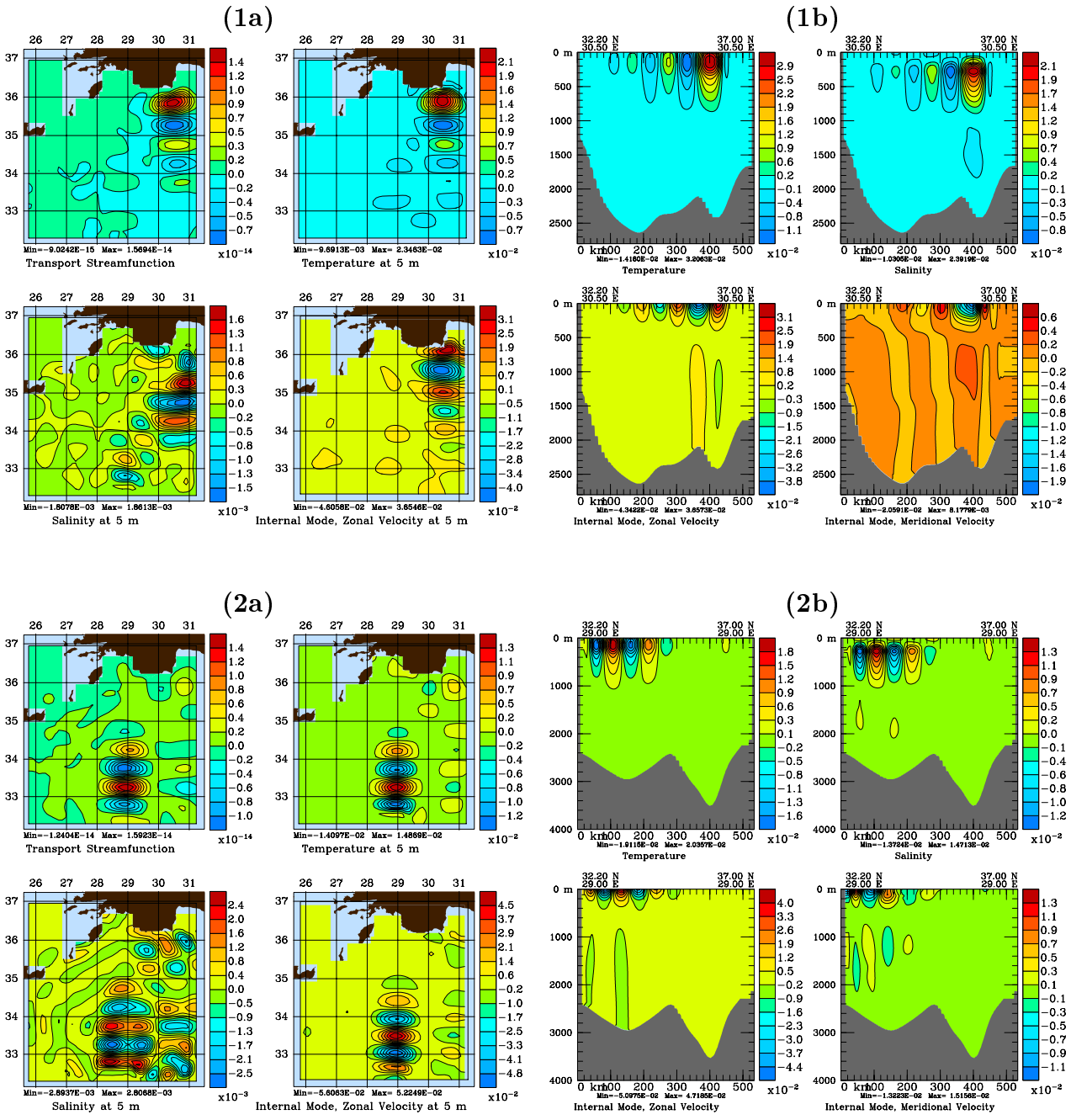

Fig. 19. As Fig. 18, but for Case 3: the vertical cross-sections are along 30.50E for vector 1, but along 29E for vector 2.

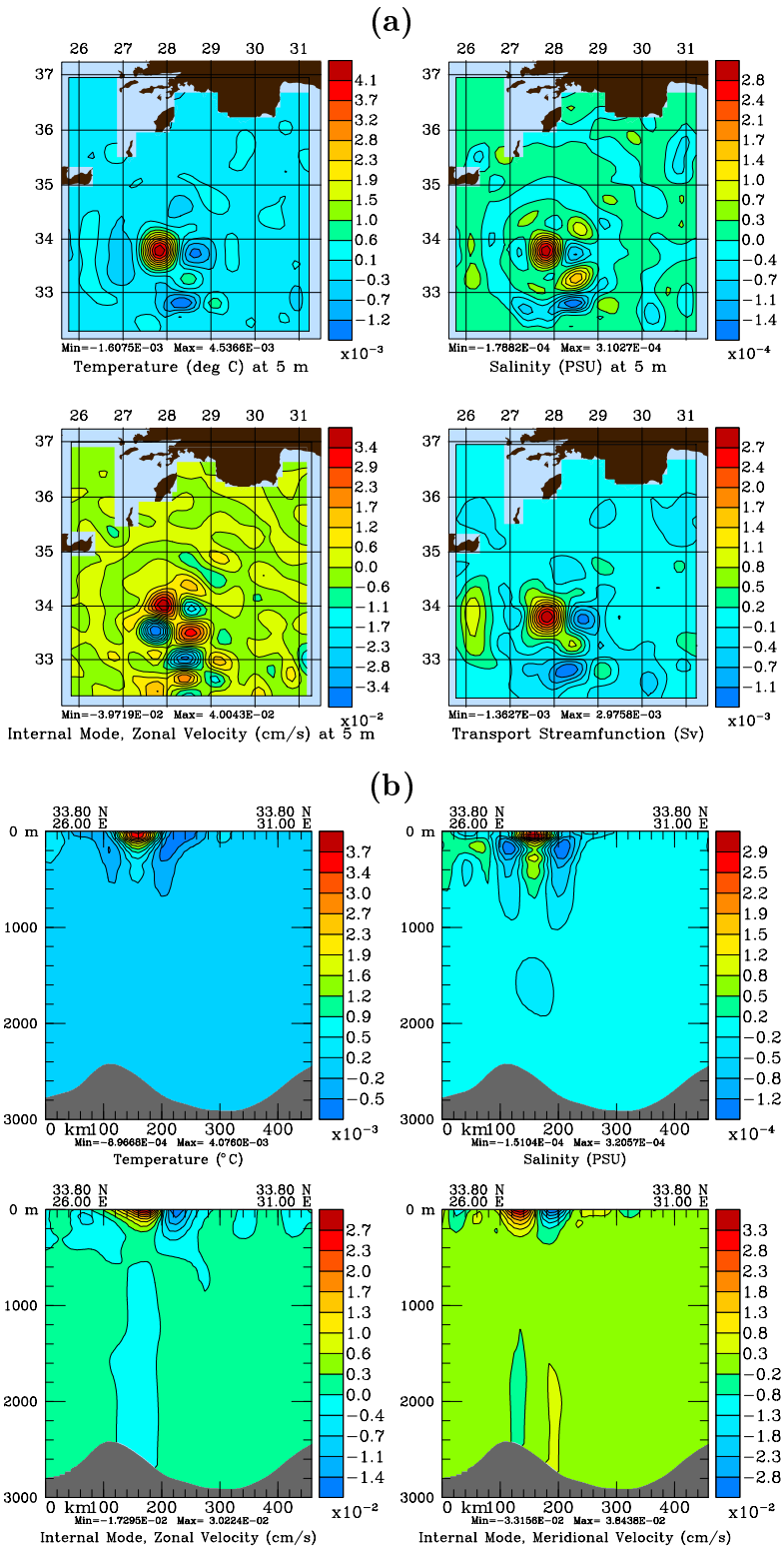

Fig. 20. As Fig. 12, but for the *a posteriori* covariance functions and for Case 3.

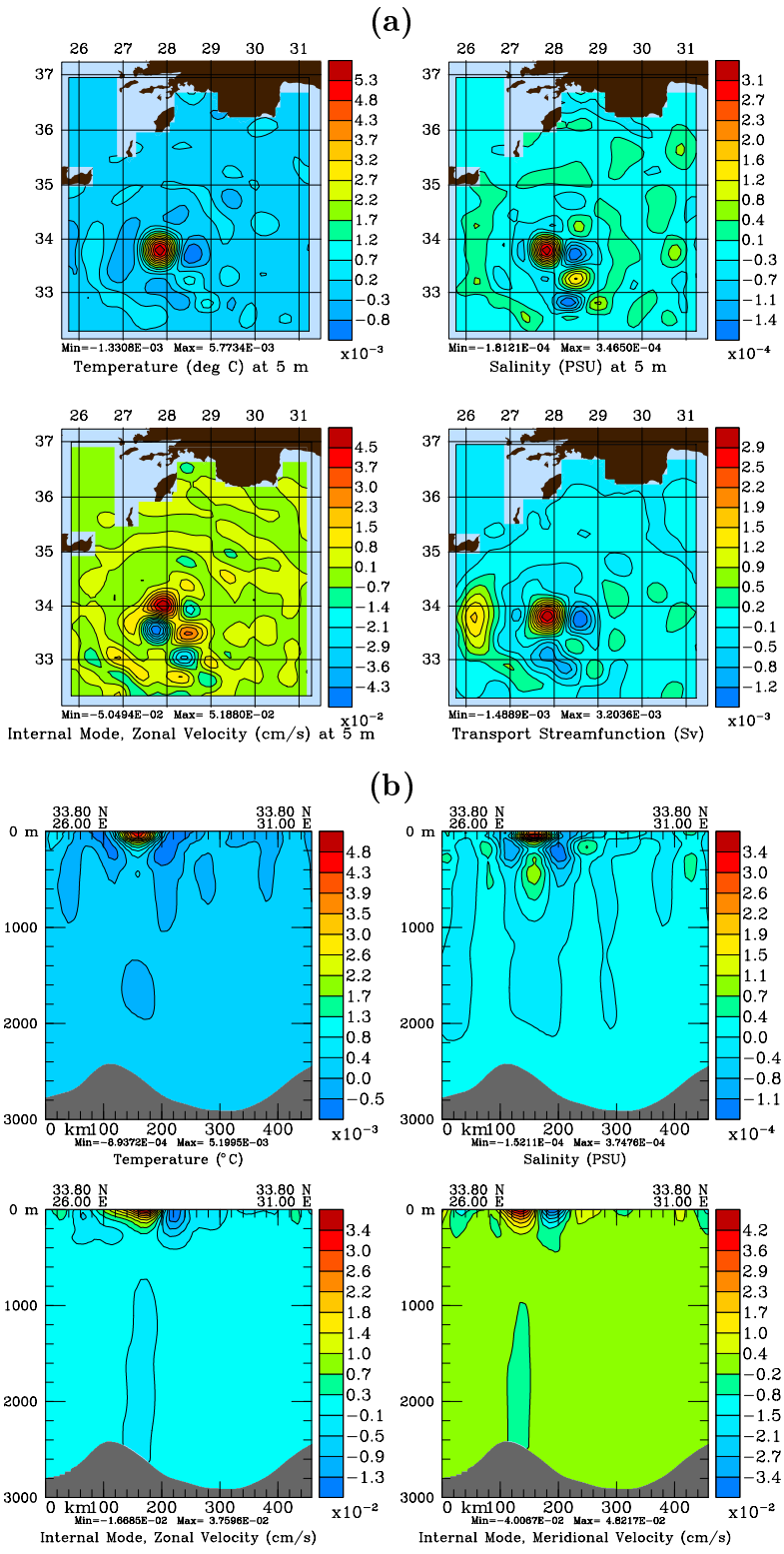

Fig. 21. As Fig. 20, but for Case 4.

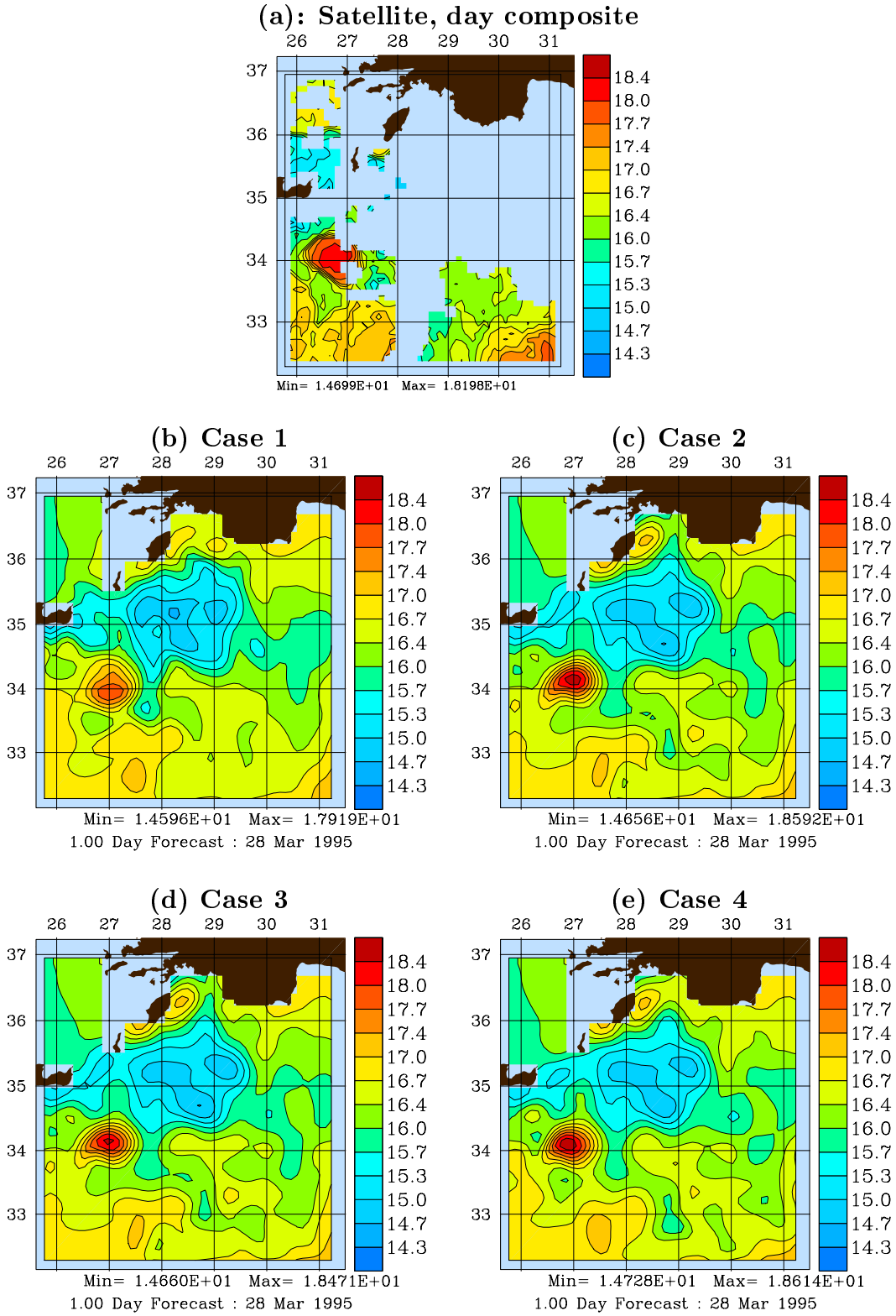

Fig. 22. (a): Satellite SST image for March 28, interpolated on the numerical grid. (b): 1-day forecast of the temperature at 5 m for Case 1. (c): as (b), but for Case 2. (d): as (b), but for Case 3. (e): as (b), but for Case 4. Note that there is almost no *in situ* data in the Aegean Sea (Fig. 9a).

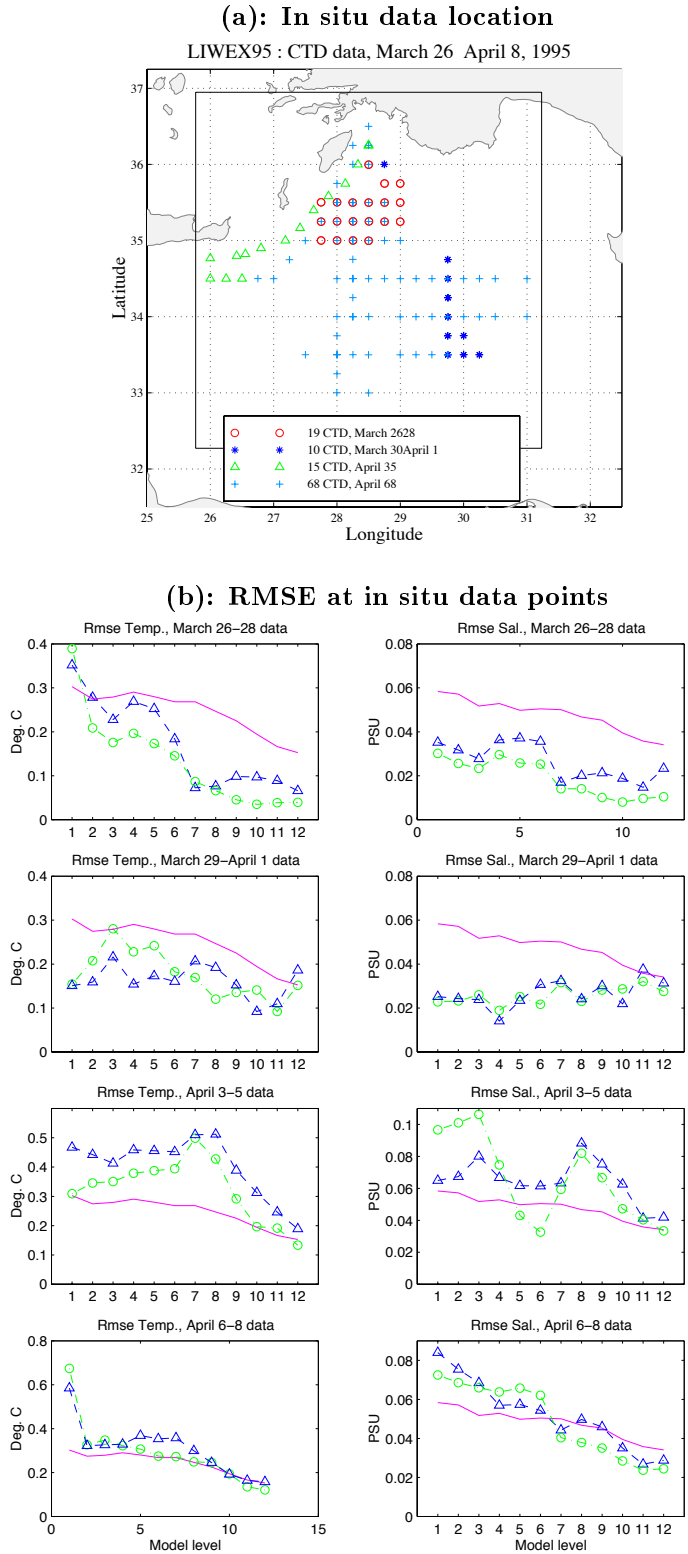

Fig. 23. (a): Sampling locations and total number of CTDs, divided in four three-day periods. (b): RMSE for temperature (left) and salinity (right) at data points, from horizontal model-level 1 (5 m) to 12 (500 m). Solid line (magenta): *a priori* model of the measurement error standard deviations (LER97). Dash-dotted line (green circles): RMSE at data point for Case 1. Dashed line (blue triangles): RMSE at data point for Case 4. Note that scales vary with the three-day periods. Cases 2 and 3, similar to Case 4, are not plotted.